Booster free from spin resonance for future 100-km-scale circular e^+e^- colliders

Tao Chen,[1,2] Zhe Duan,[1,*] Daheng Ji,[1] and Dou Wang[1]

[1]*Key Laboratory of Particle Acceleration Physics and Technology, Institute of High Energy Physics, Chinese Academy of Sciences, 19B Yuquan Road, Beijing 10049, China*

[2]*University of Chinese Academy of Sciences, 19A Yuquan Road, Beijing 10049, China*

(Received 5 March 2023; accepted 25 April 2023; published 30 May 2023)

Acceleration of polarized electron (positron) beams in a booster synchrotron may suffer from depolarization due to crossings of many spin depolarization resonances and this could limit its applications. We have studied the structure of spin depolarization resonances of a 100-km-scale booster lattice of the Circular Electron Positron Collider (CEPC). The lattice has eight arc regions with hundreds of FODO cells, interleaved with straight sections, leading to a high periodicity. Our analysis shows the contributions to the strength of intrinsic and imperfection spin resonances add up coherently near the superstrong resonances beyond 120 GeV but mostly cancel out and result in generally weak resonance strengths at lower beam energies. Detailed simulations confirm that beam polarization can be mostly maintained in the fast acceleration to 45.6 and 80 GeV but that severe depolarization may occur at even higher energies. This study suggests the possibility of acceleration of polarized electron (positron) beams to ultrahigh beam energies without the help of Siberian snakes and supports injecting highly polarized beams into the collider rings as an attractive solution for resonant depolarization measurements and longitudinally polarized colliding beam experiments for future 100-km-scale circular e^+e^- colliders.

DOI: 10.1103/PhysRevAccelBeams.26.051003

I. INTRODUCTION

The Circular Electron Positron Collider (CEPC) [1–3] is one of the future e^+e^- collider projects [4–6] that aim to study the properties of the Higgs boson, a crucial cornerstone of the Standard Model. In the Conceptual Design Report (CDR) [2] released in 2018, the CEPC was designed as a 100-km-scale double-ring collider to provide unprecedented high luminosity at center-of-mass energies of 91 GeV (Z-factory), 160 GeV (W-factory), and 240 GeV (Higgs-factory via $e^+e^- \to ZH$), upgradable to 360 GeV (ttbar energy). This powerful instrument should not only be used for precision measurements of the properties of these elementary particles but also for the search for new physics. Beam polarization is a key aspect of the CEPC design. On one hand, transverse beam polarization of at least 5% to 10% is needed to carry out resonant depolarization (RD) measurements [7,8] which are essential for beam energy calibration at Z and W energies. On the other hand, longitudinally polarized colliding beams could provide an extra probe for precision tests of the Standard Model and the search for new physics via colliding beam experiments. This application requires 50% or more longitudinal polarization at the interaction points (IPs) without significantly reducing the luminosity [9]. A pair of spin rotators would be inserted around each IP to realize the longitudinal polarization. To this end, solenoid-based spin rotators have been successfully included in the CEPC CDR lattice at Z energies [10].

There are two main approaches for preparing polarized beams to satisfy these needs. The first is to utilize the spontaneous polarization build-up in the collider rings due to the emission of synchrotron radiation, namely, the Sokolov-Ternov effect [11]. This approach has been studied [12] to provide a few percent of vertical beam polarization for the RD measurements at CERN's Future Circular e^+e^- collider (FCC-ee) [13]. The other approach is to generate polarized beams from the source and inject them into the collider rings, with the potential for achieving higher levels of beam polarization without significantly sacrificing the luminosity.

The CEPC injector chain, as outlined in the CEPC CDR [2], includes unpolarized electron and positron sources, a 10-GeV main linac, a full energy booster, and transfer lines. The booster and the collider rings share the same tunnel and the booster accelerates both electron and positron beams from 10 GeV up to the working beam energies in an alternating manner. The feasibility of extending this design

*duanz@ihep.ac.cn

to cover the generation and transport of polarized beams throughout the injector is being explored [9]. A polarized electron gun can be added to produce electron beams with 80% or more polarization [14,15]. However, the development of polarized positron sources that can simultaneously meet the requirements of high polarization, nC-level bunch charge, and high repetition rate is still a technical challenge [16]. Nevertheless, it is still possible to generate 20% or more beam polarization in the positron damping ring through the Sokolov-Ternov effect for RD measurements [9]. Maintaining the beam polarization throughout the injection chain, including the 100-km-scale booster, is essential. Previous studies for the SLC [17] and ILC [18] have shown small polarization loss in the linac and transfer lines, but the main concern is the potential polarization loss during acceleration in the booster. This is the focus of this paper.

In a high-energy electron (positron) circular accelerator, the precession of the single-particle spin expectation value $\vec{S}$, and of the unit-length spin vector $\hat{S} = \vec{S}/|\vec{S}|$, of an electron (positron), follows the Thomas-BMT equation [19,20],

$$\frac{d\hat{S}}{d\theta} = [\vec{\Omega}_0(\theta) + \vec{\omega}(\vec{u};\theta)] \times \hat{S}. \tag{1}$$

with

$$\vec{\Omega}_0(\theta) = \vec{\Omega}_{00}(\theta) + \Delta\vec{\Omega}(\theta), \tag{2}$$

where $\vec{\Omega}_0(\theta)$ is the spin precession vector on the closed orbit at the azimuthal angle θ. $\vec{\Omega}_{00}(\theta)$ and $\Delta\vec{\Omega}(\theta)$ represent the effect of electromagnetic fields on the design orbit and the impact of magnetic errors and correction fields on the spin precession vector, respectively. The vector $\vec{\omega}(\vec{u};\theta)$ describes the influence of fields seen by particles oscillating around the closed orbit with the phase space vector $\vec{u}$. In the Frenet-Serret coordinate system with a right-hand basis $(\vec{e}_x, \vec{e}_y, \vec{e}_z)$, pointing radially outwards, vertically upwards, and longitudinally (clockwise), respectively, the phase space coordinate is expressed as $\vec{u} = (x, p_x, y, p_y, z, \delta)$. x and y are the horizontal and vertical coordinates of the particle, respectively. The transverse phase-space momenta P_x and P_y are normalized by the reference momentum P, i.e., $p_x = P_x/P$ and $p_y = P_y/P$, respectively. $z = -\beta c\Delta t$ where Δt is the time difference between the particle and the reference particle arriving at the azimuthal angle θ. $\beta = v/c$, where v and c are the velocities of the particle and light, respectively. $\delta = \Delta E/E$ is the relative deviation from the design energy E. The polarization of an electron bunch is the ensemble average of the $\hat{S}$ of the particles in the bunch.

On the closed orbit, $\vec{\Omega}_0(\theta)$ is one-turn periodic so that there is a unit-length periodic solution of Eq. (1), $\hat{n}_0(\theta)$ with $\hat{n}_0(\theta + 2\pi) = \hat{n}_0(\theta)$. A spin vector that is not parallel to $\hat{n}_0$ precesses around $\hat{n}_0$ by an angle $2\pi\nu_0$ in one revolution, where ν_0 is the closed-orbit spin tune. In a circular accelerator designed with a planar geometry and without solenoid fields (hereafter referred as the "planar ring"), $\hat{n}_0$ is close to the vertical direction, and $\nu_0 \approx G\gamma$, where $G = 0.00115965219$ for electrons (positrons), and γ is the relativistic factor for the design energy E.

Away from the closed orbit, $\hat{n}_0(\theta)$ is generalized to the special solution of Eq. (1), namely, the field of vectors $\hat{n}(\vec{u};\theta)$ called the invariant spin field [21], obeying the periodicity condition $\hat{n}(\vec{u};\theta + 2\pi) = \hat{n}(\vec{u};\theta)$. Assuming that the orbital motion is integrable, then $\vec{u}$ can be expressed in terms of action-angle variables, and we denote the amplitude of the combined betatron-synchrotron motion as $\vec{I} = (I_I, I_{II}, I_{III})$ with I, II, and III denoting the three eigenmodes, which reduces to $\vec{I} = (I_x, I_y, I_z)$ in the case of weak couplings, where x, y, and z represent the horizontal, vertical, and longitudinal dimensions, respectively. The rate of spin precession around $\hat{n}$ is described by the amplitude-dependent spin tune (or spin tune in short) $\nu_s(\vec{I})$ [21]. The projection of the spin vector of a particle onto $\hat{n}$ is an adiabatic invariant $J_s = \hat{S} \cdot \hat{n}$ [22]. For typical orbital amplitudes with electrons, $\nu_s(\vec{I}) \approx \nu_0$.

In a planar ring, $\vec{\Omega}_{00}$ is dominated by the vertical guiding magnetic fields on the design trajectory. In contrast, $\Delta\vec{\Omega}$ and $\vec{\omega}$ contain contribution from machine imperfections and orbital oscillations, respectively. These contributions might perturb the particle spin motion in a resonant manner when the spin-orbit coupling resonances (spin resonances in short) condition is nearly satisfied,

$$\nu_s = K = k + k_x\nu_x + k_y\nu_y + k_z\nu_z, \tag{3}$$

where K denotes the location of the resonance, $k, k_x, k_y, k_z \in \mathbb{Z}$. ν_x, ν_y, and ν_z are the horizontal, vertical betatron tunes, and the synchrotron tunes, respectively, which are conventionally used in the case of weak couplings, reduced from the more general orbital tunes ν_I, ν_{II}, and ν_{III} obtained from the orbital eigenanalysis [23]. $\hat{n}(\vec{u};\theta)$ deviates from $\hat{n}_0(\theta)$ near these spin resonances. Spin resonances with $\nu_0 = k, k \in \mathbb{Z}$, are called integer spin resonances. In an imperfect ring, $\vec{n}_0$ could strongly deviate from the vertical direction near these integer spin resonances. Spin resonances with $|k_x| + |k_y| + |k_z| = 1$ and $|k_x| + |k_y| + |k_z| > 1$ are called first-order spin resonances and higher-order spin resonances, respectively. As we elaborate later, in the context of polarized beam acceleration in an imperfect planar ring, two families of spin resonances are most important. The integer spin resonances $\nu_0 = k$ in the tilt of $\vec{n}_0$, mainly driven by the horizontal magnetic fields that arise from vertical orbit offsets in quadrupoles as well as dipole roll errors, are also conventionally called the "imperfection resonances" [24,25]. The first-order "parent" spin resonances $\nu_0 = k \pm \nu_y$, driven by horizontal magnetic fields that arise from vertical betatron oscillations in

quadrupoles, are also conventionally called the "intrinsic resonances" [24].

In booster synchrotrons, as the particle energy is ramped up, so are the closed-orbit spin tune ν_0 and the spin tunes $\nu_s(\vec{I})$ of the particles. This leads to crossings of the underlying spin resonances and in the case of nonadiabatic spin resonance crossing, a possible consequent decrease in the $J_s = \hat{S} \cdot \hat{n}$ of the particles, and thus depolarization. If the closed-orbit spin tune, ν_0, changes linearly at the rate $\alpha = \frac{d\nu_0}{d\theta} \approx \frac{dG\gamma}{d\theta}$, the depolarization in crossing a single spin resonance at $\nu_0 = K$ can be estimated with the Froissart-Stora formula [26]

$$\frac{P_f}{P_i} \approx 2 \exp\left(-\frac{\pi|\tilde{\epsilon}_K|^2}{2\alpha}\right) - 1 \tag{4}$$

where P_i and P_f are the polarizations before and after the resonance crossing, and $\tilde{\epsilon}_K$ is the spin resonance strength, which depends on the lattice design and machine imperfections. Its detailed methods of calculation will be described later. We can identify three parameter regimes in the value of $|\tilde{\epsilon}_K|/\sqrt{\alpha}$. First, if the resonance is very strong, or when the acceleration is very slow, say $|\tilde{\epsilon}_K|/\sqrt{\alpha} > 1.84$, then $|\frac{P_f}{P_i}| > 99\%$ but with a change of sign relative to the initial value, i.e., a "spin flip," and we call this the "slow crossing" regime. Second, if the resonance is very weak, or when the acceleration is very fast, say $|\tilde{\epsilon}_K|/\sqrt{\alpha} < 0.056$, then $\frac{P_f}{P_i} > 99\%$, and we call this the "fast crossing" regime. Third, if both conditions are not satisfied, $|\frac{P_f}{P_i}|$ is reduced, and we call this the "intermediate" regime. The above analysis is for the polarization of a single particle, but it is crucial for the overall understanding of the maintenance of beam polarization in high-energy booster synchrotrons. In these types of accelerators, there are numerous spin resonances that must be crossed during acceleration. It is convenient to use Eq. (4) to evaluate the polarization loss due to the crossing of each spin resonance if the distances between the locations of adjacent spin resonances are much larger than the strengths of these spin resonances. This method allows for identifying the major spin resonances that may cause significant depolarization, before conducting more detailed simulation studies. Generally speaking, depolarization during acceleration is a significant concern in the maintenance of polarization in high-energy booster synchrotrons.

In the acceleration of polarized proton beams in the ZGS [27], the AGS, [28] and RHIC [29], the crossings of some spin resonances are in the "intermediate" regime where significant depolarization could occur. To mitigate this, various techniques have been proposed and implemented, such as tune jump [27], ac dipole [30], and the use of Siberian snakes [31]. A Siberian snake is a device that rotates spins by π around a specified axis in the horizontal plane while perturbing the orbital motion only moderately. When introduced into a circular accelerator, certain setups of Siberian snakes can make the closed-orbit spin tune ν_0 independent of the beam energy at 0.5, avoiding the crossing of imperfection and first-order spin resonances during acceleration. Partial snakes [32], which rotate spin by a fraction of π around a horizontal axis, can also be used to mitigate weak spin resonances [33]. Partial snakes and full snakes have been implemented in the AGS and RHIC, respectively, allowing for maintaining high proton beam polarization of over 50% up to 255 GeV [34]. However, higher-order spin resonances would still be encountered in the presence of snakes, leading to significant polarization loss at even higher beam energies, as seen in the studies for HERA-p [35].

To the best of our knowledge, there have been only a few experiments of polarized electron acceleration up to a few GeV beam energies, in VEPP-2M [36], ELSA [37], and VEPP-4M [38,39], with only a few spin resonances being crossed in each case. Some of these experiments were within the "slow crossing" regime. Note that with the very slow resonance crossing rate α, radiative spin diffusion, which is absent in proton synchrotrons, could lead to incomplete spin flip [40]. To avoid this, in Ref. [38], a partial snake using the detector solenoids was used to preserve the beam polarization. In the future 100-km-scale circular e^+e^- colliders like the CEPC and FCC-ee, hundreds of imperfection and intrinsic spin resonances will be encountered during the acceleration process in the booster. To combat this, various studies [41–44] have proposed the use of different setups of (partial) Siberian snakes to mitigate depolarization. However, the practical implementation of snakes using either bending magnets or solenoids is challenging due to the large size and cost required for high energy electron boosters.

In the study for the Electron Ion Collider (EIC) [45], a concept of "spin-resonance-free electron ring injector" was proposed [46] to avoid severe depolarization during acceleration to the top energy of 18 GeV. This is achieved through a clever design of the booster lattice, which features a high effective lattice periodicity of 96, placing the superstrong spin resonances beyond 18 GeV, below which the spin resonances are generally weak. The result is that the crossings of these resonances are well within the "fast crossing" regime, leading to minimal depolarization. This work highlights the importance of understanding and utilizing the structure of spin resonances.

In this work, we investigate the depolarization effects in the CEPC booster by using a simplified lattice and by incorporating preliminary error modeling and corrections. Our analysis of the structure of spin resonances reveals similarities to previous research on the EIC booster [46], with relatively weak spin resonances within the range of working beam energies. Our estimates indicate that spin resonance crossings mostly occur within the "fast crossing"

regime, resulting in minimal polarization loss during acceleration to 45.6 and 80 GeV. However, at higher energies, such as during the acceleration to 120 GeV, depolarization is more significant. These analyses are verified by multiparticle tracking simulations of the whole acceleration process. Our preliminary results were presented in [9].

This article is structured as follows: In Sec. II, we present more detailed theories of the strength of the imperfection resonances and the intrinsic resonances and analyze the structure of spin resonances of a simple model ring for both types of resonances. In Sec. III, we introduce the lattice setup of the CEPC booster. In Sec. IV, we analyze the resonance spectra for the CEPC booster lattice and estimate depolarization effects for both types of resonances. In Sec. V, we launch multiparticle tracking simulations of the beam polarization transmission in the acceleration process and compare the results to our analytical estimations. The final section summarizes our findings and suggests future studies.

II. MORE THEORIES OF THE SPIN RESONANCE STRENGTHS

Knowledge of the strength of spin resonances is essential for analyzing polarization loss using the Froissart-Stora formula. In our analysis, we focus on planar electron rings with practical machine imperfections. We first present the analysis of the strengths of imperfection resonances and intrinsic resonances. In a planar ring, the spin motion can be analyzed using a perturbative approach [47] and Fourier expansion of spin perturbations [48], which reveal the driving terms of these resonances. The corresponding Fourier component of a spin resonance can be used in place of the resonance strength in the Froissart-Stora formula.

However, determining the strength of higher-order spin resonances, which include both higher-order Fourier components and feed-up of lower-order components [35], is not straightforward. Instead, the strength of a higher-order spin resonance can be determined by retrieving the amplitude of the spin-tune jump through spin tracking of the process of resonance crossing [49]. In this paper, we use both analytical and numerical methods to determine the strengths of imperfection and intrinsic resonances of a lattice and estimate their impact on depolarization. Additionally, we evaluate the depolarization caused by these resonances and more general higher-order spin resonances, using tracking simulations that take into account the full six-dimensional orbital motion and three-dimensional spin motion.

To understand the strengths of spin resonances, we then follow the analysis of Lee's for a simplified model ring [50,51], where the strengths of imperfection and intrinsic resonances are analytically calculated in terms of the optics parameters of a basic cell, multiplied by enhancement factors that arise from the summation of periodic cells. This analysis is crucial in understanding the location of strong spin resonances and clarifying the contrast between strong resonances and weak resonances. This analysis of the structure of spin resonances will later be applied to the CEPC booster lattice in Sec. IV.

A. The strength of imperfection resonances

We denote the right-handed orthonormal set of unit-length solutions to Eq. (1) on the design orbit by $\hat{n}_{00}(\theta)$, $\hat{m}_{00}(\theta)$, and $\hat{l}_{00}(\theta)$, where $|\Delta\vec{\Omega}| = |\vec{\omega}| = 0$ and define $\hat{k}_{00}(\theta) = \hat{m}_{00}(\theta) + i\hat{l}_{00}(\theta)$. Then $\hat{k}_{00}(\theta) = e^{i[\Upsilon(\theta)-\Upsilon(\theta')]}\hat{k}_{00}(\theta')$, where $\Upsilon(\theta)$ is the spin precession phase. In a planar ring, $\Upsilon(\theta) \approx \nu_0\Phi(\theta)$, where $\Phi(\theta) = R\int_0^\theta \frac{1}{\rho_x}d\theta'$ is the integrated bending angle, R is the average radius of the ring, ρ_x is the radius of curvature for the local orbit. In a perfect planar ring, $\hat{n}_{00}(\theta)$ is vertical while $\hat{k}_{00}(\theta)$ is in the horizontal plane, respectively. Without loss of generality, we choose $(\hat{n}_{00}, \hat{m}_{00}, \hat{l}_{00})$ to be aligned with $(-\vec{e}_y, \vec{e}_x, \vec{e}_z)$, respectively, at $\theta = 0$.

In the presence of machine imperfections, we can expand $\hat{n}_0(\theta)$ as [47]

$$\hat{n}_0(\theta) \approx \hat{n}_{00}(\theta) + \mathcal{R}[c_1(\theta)\hat{k}^\star_{00}(\theta)] \tag{5}$$

Putting Eq. (5) into the Thomas-BMT equation on the closed orbit, we find

$$\frac{dc_1(\theta)}{d\theta} \approx -i\Delta\vec{\Omega}(\theta)\cdot\hat{k}_{00}(\theta) \tag{6}$$

so that

$$c_1(\theta) \approx -i\int_{-\infty}^{\theta} e^{\epsilon\theta'}\Delta\vec{\Omega}(\theta')\cdot\hat{k}_{00}(\theta')d\theta' \tag{7}$$

where now and later, $e^{\epsilon\theta'}$ denotes an infinitesimal damping factor to make the integral well behaved as $\theta' \to -\infty$ [52,53]. Note that $\vec{\Omega}(\theta)\cdot\hat{k}_{00}(\theta)e^{-i\nu_0\theta}$ is a periodic function of θ, which can be expanded into a Fourier series,

$$\Delta\Omega(\theta')\cdot\hat{k}_{00}(\theta') = \sum_{k=-\infty}^{\infty}\tilde{\epsilon}_k e^{i(\nu_0-k)\theta'} \tag{8}$$

with $\tilde{\epsilon}_k$ being the complex strength of the integer spin resonance $\nu_0 = k$,

$$\tilde{\epsilon}_k = \frac{1}{2\pi}\int_0^{2\pi}\Delta\Omega(\theta')\cdot\hat{k}_{00}(\theta')e^{-i(\nu_0-k)\theta'}d\theta' \tag{9}$$

Then, Eq. (7) can be simplified to the following form:

$$c_1(\theta) \approx -i\sum_{k=-\infty}^{\infty}\frac{\tilde{\epsilon}_k e^{i(\nu_0-k)\theta}}{\nu_0-k} \tag{10}$$

Therefore, $\tilde{\epsilon}_k$ characterizes the deviation of $\hat{n}_0$ from $\hat{n}_{00}$ near the integer spin resonances $\nu_0 = k, k \in \mathbb{Z}$.

Since $\hat{k}_{00}$ is in the horizontal plane, only the component of $\Delta\vec{\Omega}$ in the horizontal plane contributes to the $\tilde{\epsilon}_k$. In imperfect planar rings, the contribution of the radial magnetic field dominates in most cases. $\Delta\Omega_x$ denotes the component of $\Delta\vec{\Omega}$ along the $\vec{e}_x$ direction and represents the influence of the radial magnetic field ΔB_x. Its contribution to $\tilde{\epsilon}_k$ can be expressed as

$$\begin{aligned}\tilde{\epsilon}_k &\approx \frac{1}{2\pi}\int_0^{2\pi}\Delta\Omega_x(\theta')e^{i(\nu_0\Phi(\theta')-(\nu_0-k)\theta')}d\theta' \\ &= -\frac{R(1+G\gamma)}{2\pi}\int_0^{2\pi}\frac{\Delta B_x(\theta')}{B\rho}e^{ik\Phi(\theta')}d\theta', \end{aligned} \tag{11}$$

where we use the relations $\vec{e}_x(\theta')\cdot\hat{k}_{00}(\theta') = \vec{e}_x(0)\cdot\hat{k}_{00}(0)e^{i\nu_0\Phi(\theta')} = e^{i\nu_0\Phi(\theta')}$ and $\nu_0 = k$. $B\rho$ is the magnetic rigidity.

Let's denote $K = \nu_0 = k$ as the location of the imperfection resonances, whose strengths $\tilde{\epsilon}_K^{\mathrm{imp}}$ can be expressed as

$$\tilde{\epsilon}_K^{\mathrm{imp}} \approx -\frac{R(1+K)}{2\pi}\int_0^{2\pi}\frac{\Delta B_x(\theta')}{B\rho}e^{iK\Phi(\theta')}d\theta' \tag{12}$$

The radial magnetic field ΔB_x can be expanded in terms of the horizontal and vertical closed orbit x_{co} and y_{co} as,

$$\frac{\Delta B_x}{B\rho} \approx \left(\frac{\Delta B_x}{B\rho}\right)_0 + \frac{\frac{\partial B_x}{\partial x}}{B\rho}x_{\mathrm{co}} + \frac{\frac{\partial B_x}{\partial y}}{B\rho}y_{\mathrm{co}} \tag{13}$$

where the feed-down effects of multipoles are neglected, and $\frac{\frac{\partial B_x}{\partial x}}{B\rho}x_{\mathrm{co}}$ and $\frac{\frac{\partial B_x}{\partial y}}{B\rho}y_{\mathrm{co}}$ describe the influence of horizontal closed-orbit positions inside skew quadrupoles and that of vertical closed-orbit positions inside normal quadrupoles, respectively. The latter term is generally much more important. The $(\frac{\Delta B_x}{B\rho})_0$ contains the influence from various magnet misalignment errors, like vertical misalignment errors of quadrupoles and roll errors of dipoles, as well as the contribution from vertical orbital correctors.

The magnet misalignment errors can be grouped into two different categories: random and systematic. Random misalignment errors typically have zero mean and their contributions to $\tilde{\epsilon}_K^{\mathrm{imp}}$ tend to cancel out for large K. Systematic misalignment errors, on the other hand, arise from variations in the vertical magnet positions after the smoothing procedure of alignment and uneven settling of the accelerator floor over time. Their contribution to $\tilde{\epsilon}_K^{\mathrm{imp}}$ does not simply average out. Note that these two categories of magnet misalignment errors also have different influences on the patterns of the orbital correctors and their contribution to $\tilde{\epsilon}_K^{\mathrm{imp}}$. In this paper, we focus on the random errors, the treatment of the systematic errors will be pursued in a separate study. Then $\tilde{\epsilon}_K^{\mathrm{imp}}$ can be approximately by

$$\tilde{\epsilon}_K^{\mathrm{imp}} \approx -\frac{R(1+K)}{2\pi}\int_0^{2\pi}\frac{\frac{\partial B_x}{\partial y}}{B\rho}(\theta')y_{\mathrm{co}}(\theta')e^{iK\Phi(\theta')}d\theta' \tag{14}$$

This agrees with the result obtained via the spinor algebra in Refs. [24,51].

B. The strength of intrinsic resonances

We denote the right-handed orthonormal set of unit-length solutions to Eq. (1) on the closed orbit by $[\hat{n}_0(\theta), \hat{m}_0(\theta), \hat{l}_0(\theta)]$, where $|\Delta\vec{\Omega}| \neq 0$ while $|\vec{\omega}| = 0$, and define $\hat{k}_0(\theta) = \hat{m}_0(\theta) + i\hat{l}_0(\theta)$. $\hat{k}_0$ is quasiperiodic, $\hat{k}_0(\theta+2\pi) = e^{i2\pi\nu_0}\hat{k}_0(\theta)$.

When $|\Delta\vec{\Omega}| \neq 0$, $|\vec{\omega}| \neq 0$, $\hat{n}(\vec{u};\theta)$ can be expressed by [47]

$$\hat{n}(\vec{u};\theta) = \hat{n}_0(\theta)\sqrt{1-|\zeta(\vec{u};\theta)|^2} + \mathcal{R}[\hat{k}_0^{\star}(\theta)\zeta(\vec{u};\theta)], \tag{15}$$

where $\zeta(\vec{u}(\theta);\theta)$ satisfies

$$\frac{d\zeta}{d\theta} = -i\vec{\omega}\cdot\hat{k}_0\sqrt{1-|\zeta|^2} + i\vec{\omega}\cdot\hat{n}_0\zeta \tag{16}$$

For spin resonances up to the first order, the solution for $\zeta(\vec{u}(\theta);\theta)$ can be expressed as

$$\zeta(\vec{u};\theta) \approx -i\int_{-\infty}^{\theta}e^{\epsilon\theta'}\vec{\omega}(\theta')\cdot\hat{k}_0(\theta')d\theta' \tag{17}$$

Here $\vec{\omega}$ can be linearized with respect to the coordinates of the betatron oscillations x_{osc} and y_{osc} as well as the synchrotron oscillation δ_{osc} and decomposed into three oscillation modes:

$$\vec{\omega} = \vec{\omega}_z\delta_{\mathrm{osc}} + \vec{\omega}_x x_{\mathrm{osc}} + \vec{\omega}_y y_{\mathrm{osc}} \tag{18}$$

For instance, we can express r_{osc} with $r = x, y$, in terms of the action-angle variables I_r and ψ_r as

$$r_{\mathrm{osc}} = \sqrt{2I_r\beta_r}\cos(\psi_r + \tilde{\Psi}_r) \tag{19}$$

and where β_r is the betatron function and $\tilde{\Psi}_r(\theta) = \nu_r(\phi_r(\theta)-\theta)$, with $\phi_r(\theta) = \frac{R}{\nu_r}\int_0^{\theta}\frac{d\theta'}{\beta_r(\theta')}$. The solution of the oscillatory motion is $\psi_r = \psi_{r0} + \nu_r\theta$. Then Eq. (17) can be analyzed for each of these oscillation modes

$$\zeta_r(I_r,\psi_r;\theta) = -i\sum_{\pm}\int_{-\infty}^{\theta}\vec{\omega}_r\cdot\hat{k}_0\sqrt{\frac{I_r\beta_r}{2}}e^{\pm i(\psi_r+\tilde{\Psi}_r)}d\theta' \tag{20}$$

The integrand can be expanded into Fourier series,

$$\vec{\omega}_r\cdot\hat{k}_0\sqrt{\frac{I_r\beta_r}{2}}e^{\pm i(\psi_r+\tilde{\Psi}_r)} = \sum_{k=-\infty}^{\infty}\tilde{\epsilon}_{k,\pm}^{r}e^{i(\nu_0\pm\nu_r-k)\theta'} \tag{21}$$

with $\tilde{\epsilon}^r_{k,\pm}$ being the complex strength of the first-order spin resonance $\nu_0 \pm \nu_r = k, k \in \mathbb{Z}$,

$$\tilde{\epsilon}^r_{k,\pm} = \frac{1}{4\pi}\int_0^{2\pi} \vec{\omega}_r \cdot \hat{k}_0 \sqrt{2I_r\beta_r} e^{i[\pm(\psi_r+\tilde{\Psi}_r)-(\nu_0\pm\nu_r-k)\theta']} d\theta' \tag{22}$$

Then Eq. (20) can be simplified to the following form:

$$\zeta_r(I_r,\psi_r;\theta) = -\sum_{\pm}\sum_{k=-\infty}^{\infty} \frac{\tilde{\epsilon}^r_{k,\pm} e^{i(\nu_0\pm\nu_r-k)\theta'}}{\nu_0 \pm \nu_r - k} \tag{23}$$

Therefore, $\tilde{\epsilon}^r_{k,\pm}$ is a measure of the deviation of $\hat{n}$ from $\hat{n}_0$ near the first-order spin resonances $\nu_0 \pm \nu_r = k, k \in \mathbb{Z}$. This analysis can also be extended for the synchrotron oscillation mode and the first-order spin resonance $\nu_0 \pm \nu_z = k, k \in \mathbb{Z}$, obtaining a result similar to Eqs. (22) and (23) with r replaced by z.

In ideal planar rings, $\vec{k}_0$ is in the horizontal plane so that $\vec{\omega}_x \cdot \vec{k}_0$ and $\vec{\omega}_z \cdot \vec{k}_0$ vanish. Then the strengths of first-order "parent" spin resonances $\nu_0 \pm \nu_x = k, k \in \mathbb{Z}$ and $\nu_0 \pm \nu_z = k, k \in \mathbb{Z}$ vanish too. In contrast, $\vec{\omega}_y \cdot \vec{k}_0 \approx R(1+a\gamma)\frac{\frac{\partial B_x}{\partial y}}{B\rho}\vec{e}_x \cdot \vec{k}_0$ makes a nonzero contribution to the strength of the first-order "parent" spin resonances $\nu_0 \pm \nu_y = k, k \in \mathbb{Z}$, which are also called the "intrinsic resonances".

Let's denote $K = \nu_0 = k \pm \nu_y$ as the location of the intrinsic resonances, whose strength $\tilde{\epsilon}^{\text{intr}}_K$ can be expressed as a function of the vertical betatron action I_y

$$\tilde{\epsilon}^{\text{intr},\pm}_K(I_y) \approx \frac{R(1+K)}{4\pi}\int_0^{2\pi} \frac{\frac{\partial B_x}{\partial y}}{B\rho}\sqrt{2I_y\beta_y} \times e^{i[K\Phi(\theta')\mp\nu_y\phi_y(\theta')\mp\psi_{y0}]} d\theta', \tag{24}$$

where we use the relations $\vec{e}_x(\theta') \cdot \hat{k}_0(\theta') \approx e^{i\nu_0\Phi(\theta')}$ and $K = \nu_0 = k \pm \nu_y$. This also agrees with the result in Refs. [24,51].

In realistic planar rings, the complex strength of these first-order spin resonances is affected by the machine imperfections. In the context of polarized beam acceleration, the intrinsic resonances are generally more detrimental in comparison to other first-order spin resonances.

C. The spin resonance structure of a model ring

Lee derived simple analytical formulas to explain the K dependence of the strengths of the intrinsic resonances and the imperfection resonances [50,51], thereby helping to reveal interesting features of the spin-resonance spectrum. Most notably, it was shown that the maximum resonance strength is determined by two enhancement factors due to the regular arc FODO cells and the periodicity of the machine, respectively.

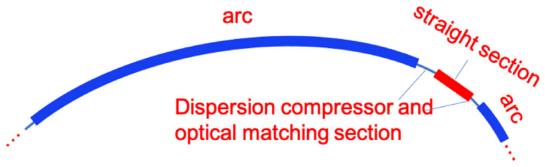

FIG. 1. Diagram of the structure of the model ring, one of P superperiods of the ring is shown.

Here, we follow these analyses [50,51] to study the structure of spin resonances for a model ring lattice with features shared with very large electron rings, and discuss the general trend of evolution of resonance strength with energy ($G\gamma$), to pave the way for the analysis of the CEPC booster lattice.

Let's consider a model ring lattice composed of P superperiods, as depicted in Fig. 1. Each superperiod includes an arc section containing M identical FODO cells with dipoles and a dispersion-free straight section containing M' identical FODO cells without dipoles. Each straight section and an adjacent arc section are connected by a dispersion suppressor and optical matching (DOM) section. Each superperiod contains two such sections in a mirror-symmetric layout. The vertical betatron phase advance of each arc FODO cell is denoted by $\phi_y^{\text{cell}} = 2\pi\mu$. Then the total vertical betatron phase advance in all FODO cells in the arc regions amounts to $2\pi\nu_B = 2\pi MP\mu$. The bending angles $\tilde{\phi}$ of dipoles in each arc FODO cell and each DOM section are $\tilde{\phi}^{\text{cell}}$ and $\tilde{\phi}^{\text{dis}}$, respectively. Let's denote the total bending angle in all arc sections as $2\pi\eta_{\text{arc}}$, then $\eta_{\text{arc}} = \frac{M\tilde{\phi}^{\text{cell}}}{M\tilde{\phi}^{\text{cell}}+2\tilde{\phi}^{\text{dis}}}$.

In addition, we assume that the vertical betatron phase advance in one straight section is $2\pi L, L \in \mathbb{Z}$. We also assume $P \ll M$ and $M' \ll M$, as in ultrahigh energy rings like the CEPC booster. Thin lens approximation for quadrupole and dipole fields is adopted so that approximations to the strength of the imperfection and the intrinsic spin resonances can be easily obtained for this model lattice layout.

1. The structure of intrinsic resonances

The strength of intrinsic resonances for this model ring can be regarded as the contribution from a superperiod $\tilde{\epsilon}^{\text{intr},\pm}_{K,0}$ multiplied by an enhancement factor $E_P^{\mp}$,

$$\tilde{\epsilon}^{\text{intr},\pm}_K = \tilde{\epsilon}^{\text{intr},\pm}_{K,0} \times E_P^{\mp}$$
$$E_P^{\mp} = e^{i\pi(P-1)\frac{K\mp\nu_y}{P}}\zeta_P\left(\frac{K\mp\nu_y}{P}\right) \tag{25}$$

which contains an enhancement function $\zeta_N(x)$ depending on an integer N and a real number x,

$$\zeta_N(x) = \frac{\sin N\pi x}{\sin \pi x} \tag{26}$$

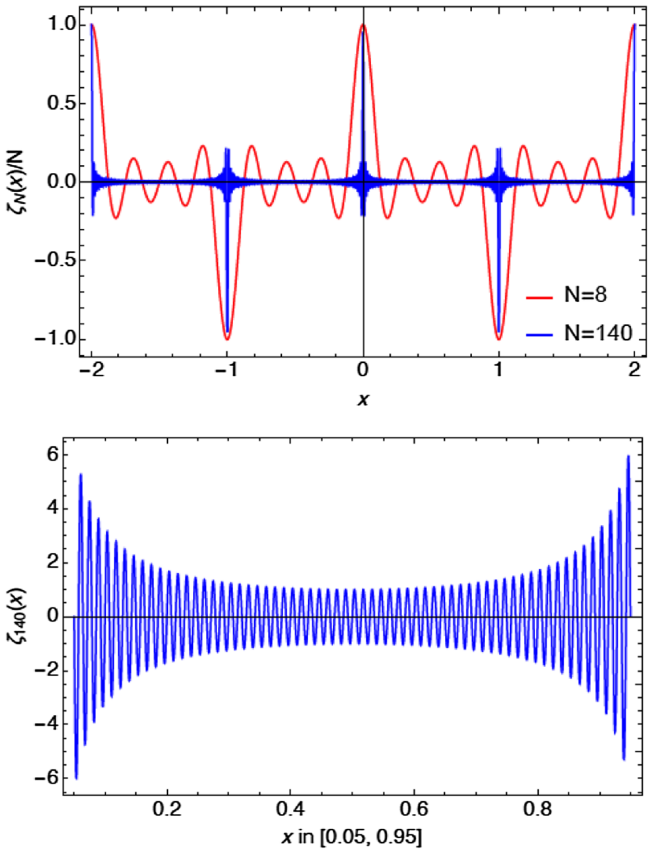

FIG. 2. The shape of the enhancement function $\zeta_N(x)$. The top plot shows $\zeta_8(x)/8$ and $\zeta_{140}(x)/140$ in the range $x \in [-2, 2]$ and the bottom plot shows $\zeta_{140}(x)$ in the range of $x \in [0.05, 0.95]$.

As shown in Fig. 2, $\zeta_N(x) = 0$ when $N * x \in \mathbb{Z}$ while $x \notin \mathbb{Z}$, and $|\zeta_N(x)| \to N$, as x approaches an integer k. In addition, for a much larger $N = 140$ relative to $N = 8$ in Fig. 2, the peaks are much narrower, and the amplitude of $\zeta_N(x)$ decays more substantially for x distant from integers. Additionally, as illustrated in the bottom plot of Fig. 2, for a large $N = 140$, when x deviates slightly from an integer by 0.05, the amplitude of $\zeta_N(x)$ is bounded within 6, less than $1/20$ of N, indicating cancelation rather than enhancement among the contributions of N identical units.

According to the form of $\zeta_N(x)$, the enhancement factor $E_P^{\mp}$ is nonzero only for the intrinsic resonances $K = nP \pm \nu_y$, $n \in \mathbb{Z}$, when the contributions from all the superperiods add up coherently, and $|E_P^{\mp}| = P$.

The contribution from one superperiod can be written as a sum of three parts,

$$\tilde{\epsilon}_{K,0}^{\mathrm{intr},\pm} = \tilde{\epsilon}_{K,0,\mathrm{arc}}^{\mathrm{intr},\pm} + \tilde{\epsilon}_{K,0,\mathrm{str}}^{\mathrm{intr},\pm} + \tilde{\epsilon}_{K,0,\mathrm{DOM}}^{\mathrm{intr},\pm} \tag{27}$$

where $\tilde{\epsilon}_{K,0,\mathrm{arc}}^{\mathrm{intr},\pm}$, $\tilde{\epsilon}_{K,0,\mathrm{str}}^{\mathrm{intr},\pm}$, and $\tilde{\epsilon}_{K,0,\mathrm{DOM}}^{\mathrm{intr},\pm}$ represent the contributions from one arc section, one straight section, as well as two DOM sections, respectively. The first two terms involve summations of contributions from many identical FODO cells and thus can be greatly simplified analytically, featuring special patterns of enhancement or cancelation under specific conditions. On the other hand, the third term depends on the specific optics design and we are not aware of any general method for simplifying it. However, the DOM sections typically cover only a small fraction of the entire lattice, in particular, in larger rings. In addition, we also find a pattern whereby these contributions tend to cancel out for small K.

First, the contribution from one arc section can be regarded as that from a standard arc FODO cell multiplied by an enhancement factor $E_M^{\mp}$ due to the M FODO cells. The simplified expression for $\tilde{\epsilon}_{K,0,\mathrm{arc}}^{\mathrm{intr},\pm}$ is

$$\tilde{\epsilon}_{K,0,\mathrm{arc}}^{\mathrm{intr},\pm} \approx \frac{1+K}{4\pi}\sqrt{2I_y}\left(g_f + g_d e^{i\frac{K\eta_{\mathrm{arc}} \mp \nu_B}{MP}\pi}\right)E_M^{\mp}$$
$$E_M^{\mp} = e^{i\pi(M-1)\frac{K\eta_{\mathrm{arc}} \mp \nu_B}{PM}}\zeta_M\left(\frac{K\eta_{\mathrm{arc}} \mp \nu_B}{PM}\right) \tag{28}$$

where

$$g = \frac{R}{B\rho}\int_{\mathrm{quad}} \frac{\partial B_x}{\partial y}\sqrt{\beta_y}\, d\theta \tag{29}$$

is an integral over a quadrupole and g_f and q_d denote the corresponding values for the focusing and defocusing quadrupoles in an arc FODO cell, respectively. According to the properties of $\zeta_N(x)$, the amplitude of the enhancement factor $|E_M^{\mp}|$ approaches M near $K = (mPM \pm \nu_B)/\eta_{\mathrm{arc}}$, $m \in \mathbb{Z}$, when the contribution from all the FODO cells in an arc add up coherently. However, $|E_M^{\mp}|$ reduces to a small fraction of M when K deviates from these conditions by a corresponding ΔK. For example, if we take $P = 8$, $M = 140$, and $\eta_{\mathrm{arc}} = 140/142$, then $|E_M^{\mp}| < 6$ for $\Delta K \geq 56.8$.

Next, the contribution from one straight section can also be regarded as that of a standard FODO cell without dipoles multiplied by an enhancement factor $E_{M'}^{\prime\mp}$ due to the M' FODO cells to give

$$\tilde{\epsilon}_{K,0,\mathrm{str}}^{\mathrm{intr},\pm} \approx \frac{1+K}{4\pi}\sqrt{2I_y}\left(g'_f + g'_d e^{i\frac{\mp\nu_{y,\mathrm{str}}}{PM'}\pi}\right)E_{M'}^{\prime\mp}$$
$$E_{M'}^{\prime\mp} = e^{i\pi(M'-1)\frac{\mp\nu_{y,\mathrm{str}}}{PM'}}\zeta_{M'}\left(\frac{\mp\nu_{y,\mathrm{str}}}{PM'}\right), \tag{30}$$

where g'_f and g'_d denote the integral defined in Eq. (29) for the focusing and defocusing quadrupoles in a standard FODO cell of the straight sections, respectively. $2\pi\nu_{y,\mathrm{str}}$ is the total vertical betatron phase advance in all straight sections. Since we assume the vertical betatron phase advance in one straight section is $2\pi L, L \in \mathbb{Z}$, $\nu_{y,\mathrm{str}} = PL$ for the model ring. According to the properties of $\zeta_N(x)$, when $M' \neq L$, $E_{M'}^{\prime\mp}$ is zero and the contribution from straight sections to the strength of intrinsic resonances vanishes.

Now, we are ready to summarize the features of the strengths of intrinsic resonances for this model ring. The straight sections have zero contribution to the resonance strength, while the DOM sections cover only a small fraction of the whole lattice. Therefore, when $|E_P^{\mp}|$ equals to P and $|E_M^{\mp}|$ is close to the maximum values so that the contributions from all PM arc FODO cells add up, the resonance strengths are greatly enhanced. We call these resonances as the superstrong intrinsic resonances. As $P \ll M$, this occurs at those $K = nP \pm \nu_y$ which are closest to $(mPM \pm \nu_B)/\eta_{\text{arc}}, m \in \mathbb{Z}$.

For a large M, away from these superstrong intrinsic resonances, the amplitude of $E_M^{\mp}$ decays rapidly, making the contributions from arc sections much weaker and those from DOM sections more significant. Additionally, there can be cancelations between the contributions from the arc sections and the DOM sections, depending on the lattice parameters. In particular, when ν_y is large and $K \ll \nu_y$, the exponential factor $e^{i[K\Phi(\theta')\mp\nu_y\phi_y(\theta')\mp\psi_{y0}]}$ in Eq. (24) includes a fast wave with a phase $\nu_y\phi_y(\theta')$ modulated by the slow wave with a phase $K\Phi(\theta')$ so that the contributions from all FODO cells in each superperiod tend to cancel out. Such a cancelation generally becomes more incomplete as K increases.

Our analysis indicates a general trend for the strengths of intrinsic resonances. For a fixed vertical betatron amplitude I_y, as K increases, we generally expect that the resonance strength increases until the first superstrong resonance is reached, after which it oscillates as adjacent superstrong resonances are approached and left behind.

In practical lattices, the straight sections may not be composed of identical FODO cells and may not have the assumed betatron phase advance. However, efficient cancelation can still occur among a large number of quadrupoles as the phase $K\Phi(\theta')$ remains almost constant in straight sections. Additionally, the unique functions of each straight section and machine-geometry considerations, such as bypasses near the interaction regions, can break lattice periodicity, resulting in some relatively weak spin resonances different from the condition $K = nP \pm \nu_y$. Nevertheless, the method of determining locations of superstrong resonances and the general trend for the strengths of intrinsic resonances are still valid.

2. The structure of imperfection resonances

The expression of the strength of imperfection resonances, in Eq. (14), includes the vertical closed orbit y_{co}, which is related to the radial magnetic field errors $(\frac{\Delta B_x}{B\rho})_0$ via the Hill's equation [51]

$$\frac{d^2(y_{\text{co}}/\sqrt{\beta_y})}{d\phi_y^2} + \nu_y^2(y_{\text{co}}/\sqrt{\beta_y}) = \nu_y^2\beta_y^{3/2}\left(\frac{\Delta B_x}{B\rho}\right)_0 \tag{31}$$

the solution for y_{co} is given by

$$y_{\text{co}}(\theta) = \beta_y(\theta)^{1/2}\sum_{k=-\infty}^{\infty}\frac{\nu_y^2 f_k e^{ik\phi_y(\theta)}}{\nu_y^2 - k^2} \tag{32}$$

where f_k is the Fourier amplitude of the error harmonic k given by

$$f_k = \frac{R}{2\pi\nu_y}\oint\sqrt{\beta_y}\left(\frac{\Delta B_x}{B\rho}\right)_0 e^{-ik\phi_y(\theta)}d\theta \tag{33}$$

The strengths of imperfection resonances can then be evaluated as [51]

$$\tilde{\epsilon}_K^{\text{imp}} \approx -\frac{R(1+K)}{2\pi}\sum_{k=-\infty}^{\infty}\frac{\nu_y^2 f_k}{\nu_y^2 - k^2}\oint\frac{\frac{\partial B_x}{\partial y}}{B\rho}\beta_y^{1/2}e^{i(k\phi_y + K\Phi)}d\theta. \tag{34}$$

The strengths of imperfection resonances of this model ring can also be written as sums of three contributions from the arc sections, the straight sections, and the DOM sections, respectively,

$$\tilde{\epsilon}_K^{\text{imp}} = \tilde{\epsilon}_{K,\text{arc}}^{\text{imp}} + \tilde{\epsilon}_{K,\text{str}}^{\text{imp}} + \tilde{\epsilon}_{K,\text{DOM}}^{\text{imp}} \tag{35}$$

The first two terms involve summations of the contributions from many identical FODO cells of different superperiods and thus can be greatly simplified analytically and feature special patterns of enhancement or cancelation under certain conditions.

First, the contribution from all arc sections can be expressed as [51]

$$\begin{aligned}\tilde{\epsilon}_{K,\text{arc}}^{\text{imp}} \approx{}& \frac{1+K}{2\pi}\sum_{k=-\infty}^{\infty}\frac{\nu_y^2 f_k}{\nu_y^2 - k^2}e^{i\frac{P-1}{P}(k+K)\pi} \\ &\times e^{i\frac{M-1}{PM}\left(K\eta_{\text{arc}}+\frac{k\nu_B}{\nu_y}\right)\pi}\left[g_d - g_f e^{-i\frac{K\eta_{\text{arc}}+\frac{k\nu_B}{\nu_y}}{MP}\pi}\right] \\ &\times \zeta_P\left(\frac{k+K}{P}\right)\zeta_M\left(\frac{K\eta_{\text{arc}} + k\frac{\nu_B}{\nu_y}}{MP}\right)\end{aligned} \tag{36}$$

For a specified k, $|\zeta_P| = P$ for $K = nP - k$, $n \in \mathbb{Z}$ so that the contributions from all superperiods add up coherently. If this condition is not met, $\zeta_P = 0$. $|\zeta_M|$ approaches M as K approaches $(mPM - k\frac{\nu_B}{\nu_y})/\eta_{\text{arc}}$, $m \in \mathbb{Z}$ so that the contributions from all FODO cells in an arc section add up coherently. Note that for each integer value of K, a family of k always exists that satisfies $K = nP - k$, $n \in \mathbb{Z}$ so that there is no complete cancelation in the strength of imperfection resonances due to the lattice periodicity unlike the case for intrinsic resonances. This can be viewed as the result of symmetry breaking due to machine imperfections.

In addition, the strengths of imperfection resonances depend on the spectrum of f_k. For an imperfect lattice

before dedicated closed-orbit correction, the most important terms are those with $|k|$ near ν_y, as the factor $|\frac{\nu_y^2}{\nu_y^2-k^2}|$ can be very large. In particular, let's consider the terms $k = \pm[\nu_y]$ where $[x]$ denotes the integer nearest to a real number x, the corresponding superstrong imperfection resonances are those when both conditions $K = mP \pm [\nu_y]$ and $K = [(nPM \pm [\nu_y]\frac{\nu_B}{\nu_y})/\eta_{\text{arc}}]$ are nearly satisfied.

Note that the closed-orbit correction can significantly change the spectrum of f_k and tends to reduce the amplitudes of f_k with $|k|$ near ν_y as well as other harmonics, in a way depending on the detailed correction algorithms and settings. Even if the superstrong imperfection resonances as described above can become less prominent after the closed-orbit correction, they are likely to be surrounded by plateaus of strong imperfection resonances.

Second, the contribution from all straight sections can also be regarded as a sum over harmonics k:

$$\tilde{\epsilon}_{K,\text{str}}^{\text{imp}} \approx \frac{1+K}{2\pi}\sum_{k=-\infty}^{\infty}\frac{\nu_y^2 f_k}{\nu_y^2-k^2}e^{i\frac{P-1}{P}(k+K)\pi} \times e^{i(M'-1)\frac{\mp\nu_{y,\text{str}}\frac{k}{\nu_y}}{PM'}\pi}\left[g_d - g_f e^{-i\frac{\mp\nu_{y,\text{str}}\frac{k}{\nu_y}}{PM'}\pi}\right] \times \zeta_P\left(\frac{k+K}{P}\right)\zeta_{M'}\left(\frac{\mp\nu_{y,\text{str}}\frac{k}{\nu_y}}{PM'}\right) \quad (37)$$

In this case, no matter what $\nu_{y,\text{str}}$ is, there will always be many k that make the enhancement factor $\zeta_{M'}$ nonzero so that the total sum will not be zero. If $M' \neq L$ and ν_y is large, since $k = \nu_y$ is a zero point of $\zeta_{M'}$, for those most important items ($|k|$ near ν_y), their corresponding $\zeta_{M'}$ will be close to zero so that the contribution of the straight section will be relatively small.

To summarize, the structure of imperfection resonances, with the contribution from only one harmonic k, is quite similar to the structure of the intrinsic resonances. Besides the peaks when the contributions from all arc FODO cells add up coherently, there is also cancelation among all FODO cells if $k \gg 1$ and $K \ll k$. Nevertheless, the strength of an imperfection resonance is the sum of various harmonics k modulated by $\frac{\nu_y^2 f_k}{\nu_y^2-k^2}$, with varying locations of enhancement and thus strongly depends on the spectrum of f_k. In general, after the closed-orbit correction, the f_k terms with $|k|$ near ν_y become weaker, the terms with $|k|$ further away from ν_y are less reduced, forming a plateau around the original peak. Generally, we expect that the strength of imperfection resonances increases with K until reaching the plateau near the first superstrong imperfection resonance, after which it oscillates as adjacent superstrong imperfection resonances are approached and left behind.

III. CEPC BOOSTER LATTICE SETUP

In this paper, we study a simplified lattice for the CEPC booster. As shown in Fig. 3, the lattice is composed of 8 identical arc sections, 8 straight sections, and 16 DOM sections connecting them. Each arc section consists of 140 standard FODO cells with a length of 71 m and 90° phase advances in both horizontal and vertical planes. The straight sections include two bypass regions near the interaction regions of the collider rings ("IR bypass" in Fig. 3), two rf regions that accommodate the rf cavities ('rf" in Fig. 3), as well as four other regions for injection and extraction and other functionalities. However, the optics design for these special functions is not implemented in this lattice. Instead, each of these straight sections contains 24 identical FODO cells with the total horizontal and vertical betatron phase advances both of $6 \times 2\pi$. Each DOM section includes a dispersion suppressor and an optics-matching region, consisting of six irregular FODO cells. The dispersion suppressor consists of two FODO cells with dipoles that have half the bending angle of normal arc dipoles. The optics-matching region consists of four FODO cells that match the optics between the dispersion suppressor and the straight section. The strengths of quadrupoles are the same in the optics-matching regions next to the bypass regions and the rf regions, while quadrupoles in the optics-matching regions next to the four other straight sections have been slightly adjusted simultaneously for fine-tuning of the betatron tunes, effectively reducing the lattice periodicity to 4. The circumference of the booster is 100016.4 m, the same as the collider rings, of which 80% is the arc region. In this paper, we discuss three operation modes of the booster with the extraction energy at 45.6 GeV in the Z mode, 80 GeV in the W mode, and 120 GeV in the H mode. The main parameters of the CEPC booster lattice at these three beam energies are listed in Table I.

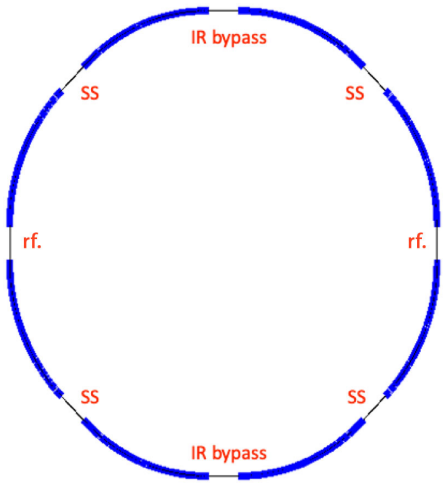

FIG. 3. Layout of the candidate lattice for the CEPC booster.

TABLE I. Parameters of the CEPC booster lattice.

Operation mode	Z	W	H
Extraction energy (GeV)	45.6	80.0	120.0
$G\gamma$ at extraction energy	103.48	181.55	272.33
Betatron tune ν_x/ν_y		353.18/353.28	
Synchrotron tune ν_z	0.1	0.1	0.13
Natural emittance $\epsilon_{\text{natural}}$ (nm)	0.19	0.58	1.29
Transverse damping time (s)	0.878	0.162	0.048
Vertical damping time (s)	0.889	0.164	0.048
Longitudinal damping time (s)	0.448	0.082	0.024

To reflect the influence of machine imperfections on beam polarization, we introduced misalignment errors and relative field errors of magnets, listed in Table II, into the lattice. Using the Accelerator Toolbox (AT) code [55], these errors were generated according to a Gaussian distribution truncated at $\pm 3\sigma$. We then performed closed-orbit correction and betatron-tune correction for these error seeds to restore the lattice performance. These error seeds were then converted to the lattice format of Bmad [56,57], for the calculations of closed orbit and optics parameters, which were then used to calculate the strength of imperfection resonances. Finally, we also used Bmad for detailed multiparticle simulations of orbital and spin motion.

For the closed-orbit correction, we imagined that there would be extra windings on the focusing and defocusing quadrupoles and used them as horizontal and vertical orbital correctors, respectively. Moreover, we assumed that BPMs are attached to all the quadrupoles, four per betatron wave period. Note that these are reasonable approximations in this preliminary analysis before more realistic modeling of the correction procedure with stand-alone correctors and BPMs is carried out. There are inevitably some differences between the magnetic centers of quadrupoles and the electric centers of adjacent BPMs, namely, the BPM offsets, and this has a substantial influence on the residual closed-orbit distortion (COD) after correction. As will be shown later, and as expected, the level of COD affects the polarization loss during the acceleration. At this stage, we are not in a position to predict what level of BPM offset or COD can be achieved for the CEPC booster. Instead, we try to explore the dependence of polarization loss on the level of COD. To this end, we introduced BPM offsets that also follow a Gaussian distribution truncated at $\pm 3\sigma$. We scanned a range of the rms BPM offset from 30 to 180 μm, with an interval of 30 μm. For each setting of rms BPM offset, we generated error seeds and carried out closed-orbit correction using the singular value decomposition (SVD) algorithm. Note that the closed-orbit correction to some error seeds failed to converge so that no closed orbit was found. These failed error seeds were simply removed. We are aware that the algorithm of closed-orbit correction can be improved by adjusting the truncation of the singular values and employing multiple iterations, but this is beyond the scope of this paper. For each setting of rms BPM offset, we accumulated ten error seeds with converged closed-orbit correction and then corrected the betatron tunes using the quadrupole knobs in the DOM sections without affecting the arc and straight sections. Then, we obtained a collection of 60 error seeds for the evaluation of the attainable polarization transmission.

TABLE II. Magnet error settings.

	Misalignment error				
Component	Δx (μm)	Δy (μm)	Δz (μm)	$\Delta\theta_z$ (μrad)	Field error
Dipole	100	100	100	100	0.05%
Quadrupole	100	100	100	100	0.02%
Sextupole	100	100	100	100	0.03%

In electron circular accelerators, the element-by-element synchrotron-radiation energy loss accumulates in the arc sections until it is compensated in the rf cavities localized in straight sections. This leads to an "energy sawtooth" for the reference particle, and a sawtooth-shape contribution to the CODs in dispersive regions, leading to optics perturbations. Hereafter, we refer to this effect as the sawtooth effect. In the above correction procedures, the element-by-element synchrotron-radiation energy loss was turned off so that the sawtooth effect was not taken into account. Figure 4 shows the horizontal and vertical rms CODs of the 60 error seeds for the case without the sawtooth effect, as well as the cases at a beam energy of 45.6, 80, and 120 GeV with the sawtooth effect. The rms vertical CODs in the case without the sawtooth effect are in the range of 80 to 220 μm. There is a general trend that the rms vertical COD correlates with the rms BPM offset, apart from a few outliers. Since the amplitude of the energy sawtooth scales with E^3, the sawtooth effect is much more pronounced at higher beam energies. Figure 4 shows that the horizontal and vertical rms CODs of the case at 45.6 GeV with the sawtooth effect are very close to the results of the case without the sawtooth effect, while the difference between the cases with and without the sawtooth effect becomes more substantial at 80 and 120 GeV. Since the amplitude of the vertical dispersion is generally much smaller than the horizontal dispersion, the influence of the sawtooth effect on the vertical rms COD is less severe relative to that on the horizontal rms COD. As we will elaborate later in this paper, this difference in the vertical rms COD also affects the calculation of the strength of imperfection resonances and thus the estimation of the depolarization during the acceleration.

Figure 5(a) shows the vertical equilibrium emittances $\epsilon_{y,\text{eq}}$ and the ratios between the transverse equilibrium emittances $\kappa = \epsilon_{y,\text{eq}}/\epsilon_{x,\text{eq}}$, for the 60 error seeds at a beam energy of 120 GeV, calculated using the beam envelope formalism [58] implemented in Bmad, which takes into account of the sawtooth effect. $\epsilon_{y,\text{eq}}$ is in the range of 6 pm to about 500 pm, and κ lies between 0.49% and 34.8%

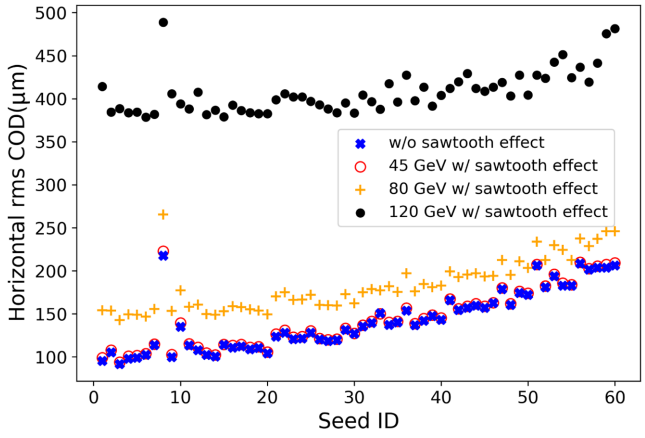

(a) Horizontal rms CODs

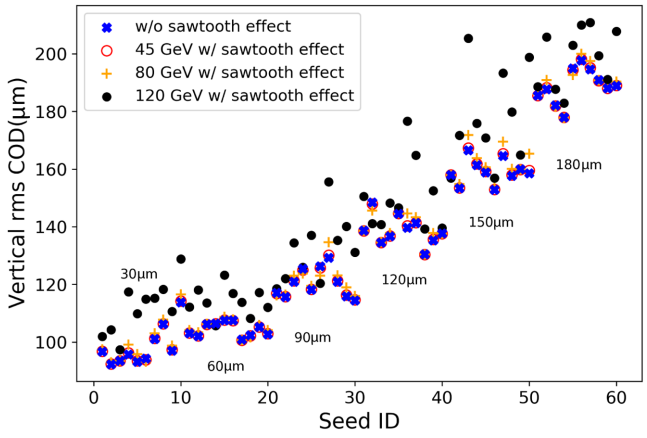

(b) Vertical rms CODs

FIG. 4. rms CODs of the 60 error seeds after correction for the case without the sawtooth effect as well as the cases with the sawtooth effect at three different beam energies, (a) and (b) show the rms CODs in the horizontal and vertical planes, respectively. The rms BPM offsets for each subset of error seeds are marked in (b).

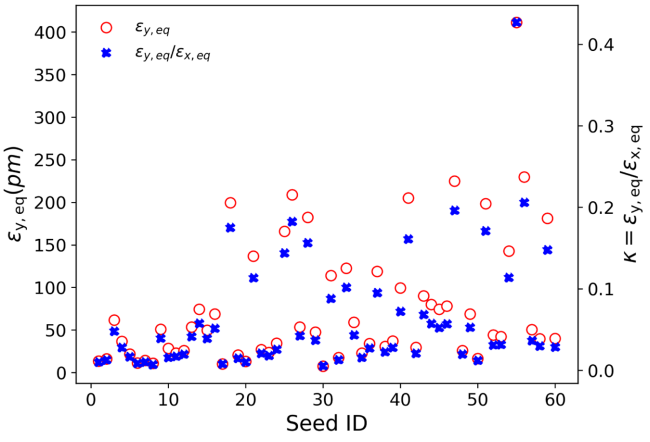

(a)

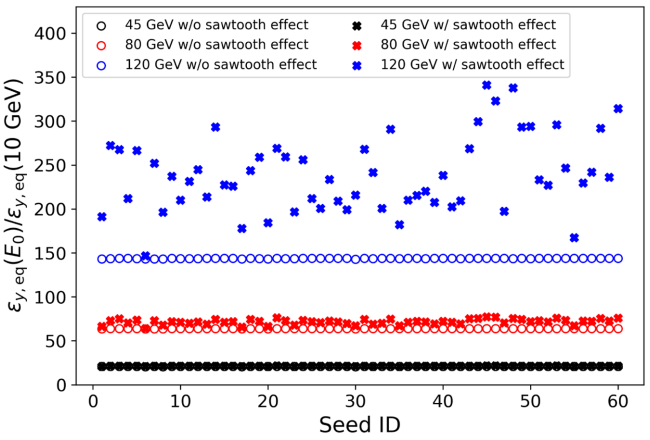

(b)

FIG. 5. The equilibrium emittances of the 60 error seeds. (a) Vertical equilibrium emittance and the ratio between transverse equilibrium emittances at 120 GeV. (b) Ratio of the vertical equilibrium emittance at different energies relative to that at 10 GeV, for the cases without and with sawtooth effect, respectively.

among the error seeds. Dedicated optics corrections, in particular, the dispersion-free steering [59] and coupling correction [60], can in principle be implemented to reduce κ to a few percent or even lower. Nevertheless, this study aims to show how the vertical equilibrium emittance would affect the polarization transmission in the booster. The necessity and the method of implementing the low emittance tuning are beyond the scope of this paper. In addition, without the sawtooth effect, $\epsilon_{y,\mathrm{eq}}(E)$ is proportional to E^2, while with the sawtooth effect, the change in the vertical dispersion and transverse coupling would alter this proportion. Figure 5(b) shows $\epsilon_{y,\mathrm{eq}}(E)/\epsilon_{y,\mathrm{eq}}(10\ \mathrm{GeV})$ at the three extraction beam energies for the 60 error seeds, with and without the sawtooth effect, respectively. The difference between the cases with and without the sawtooth effect becomes clear at higher beam energies above 80 GeV.

The time dependence of the energy ramping is also very relevant for the study of beam polarization evolution in the booster. Following the CEPC CDR, we adopted a cosine-shaped energy ramping curve

$$E(t) = E_{\mathrm{inj}} + \frac{(E_{\mathrm{ext}} - E_{\mathrm{inj}})}{2}\left[1 - \cos\left(\frac{\pi t}{t_{\mathrm{ramp}}}\right)\right] \quad (38)$$

With this, we fixed the booster injection energy to 10 GeV and set the ramping time t_{ramp} to 1.9, 3.3, and 5.0 s for the acceleration to 45.6 (Z mode), 80 (W mode), and 120 GeV (H mode), respectively. The rf voltages and phases were set to compensate for the synchrotron radiation energy loss during the ramp, as well as for maintaining a fixed synchrotron tune, as listed for different extraction energies in Table I. Accordingly, for the bare lattice, we can evaluate the spin tune on the design orbit $G\gamma(t)$, as well as the resonance crossing rate $\alpha(t)$,

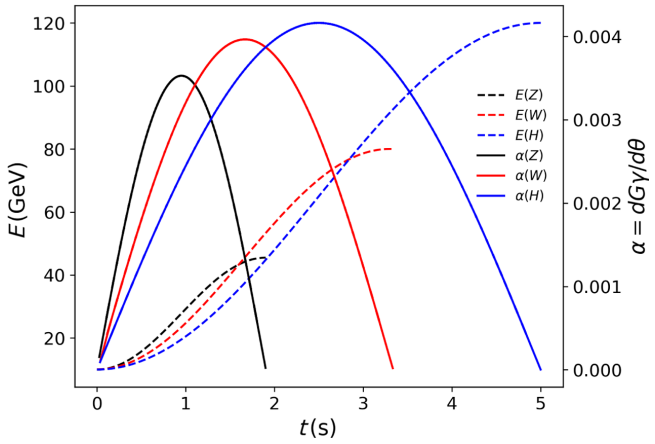

FIG. 6. The evolution of the beam central energy (in dashed lines) and the spin-resonance crossing rate α (in solid lines) for the three different operation modes.

$$G\gamma(t) = \frac{E[\mathrm{GeV}](t)}{0.4406485}$$
$$\alpha(t) \approx \frac{d[G\gamma(t)]}{d\theta} \tag{39}$$

Note that the beam particles also execute synchrotron oscillations in the acceleration process, which would modify the resonance crossing rate, in particular, near the injection and extraction beam energies when the energy ramping rate is lower. Figure 6 shows the evolution of the beam energy and the resonance crossing rate during the acceleration process for the three different operation modes. Due to the large circumference of the CEPC booster, the resonance crossing rate is above 0.001 most of the time during the acceleration process so that according to the Froissart-Stora formula, the crossings of spin resonances with $|\tilde{\epsilon}| < 0.019$ are within the fast crossing regime.

Moreover, in the analysis and simulations of the evolution of the beam polarization, we assume the injected beam has a six-dimensional Gaussian distribution, with a transverse distribution matched to the Courant-Snyder parameters at the injection point of the booster lattice. The injected beam parameters are listed in Table III, where the transverse rms emittances are more conservative than the specifications outlined in the CEPC CDR.

After injection into the booster, the evolution of the vertical rms beam emittance $\epsilon_{y,\mathrm{rms}}(t)$ can be approximated following [61] as

TABLE III. Parameters of the booster injected beam.

Injection beam energy (GeV)	10.0
rms energy spread (%)	0.16
rms bunch length (mm)	1.0
Horizontal and vertical rms emittance (nm)	80/40

$$\frac{d\epsilon_y^N(t)}{dt} = -\left[\frac{1}{E(t)}\frac{dE(t)}{dt} + \frac{2}{\tau_{y,0}}\left(\frac{E(t)}{E_0}\right)^3\right]\epsilon_y^N(t) + \frac{2}{\tau_{y,0}}\left(\frac{E(t)}{E_0}\right)^5 \tag{40}$$

where $\epsilon_y^N = \epsilon_{y,\mathrm{rms}}(t)/\epsilon_{y,\mathrm{eq},0}$, and $\epsilon_{y,\mathrm{eq},0}$, and $\tau_{y,0}$ are the vertical equilibrium emittance and the radiation damping time at the reference energy $E_0 = 120$ GeV, respectively. This equation accounts for the combined effects of adiabatic damping, radiation damping, and quantum excitation. Including the sawtooth effect is not straightforward and is ignored here, though its influence is not necessarily negligible, as illustrated by Fig. 5(b). Given the initial vertical rms emittance, Eq. (40) can be solved numerically to obtain the evolution of the vertical rms emittance during the acceleration.

A more realistic way to evaluate the evolution of the vertical rms emittance is to carry out multiparticle simulations. For this, we used the "long_term_tracking" program [62] of Bmad to simulate the acceleration process. We set the ramping curve of the beam energy and the rf parameters and turned on the radiation damping and quantum excitation in the element-by-element tracking. We tracked a Gaussian beam with 1000 particles with the initial parameters specified in Table III and computed the eigenemittances along the ramp. For error seed 001 from the collection, the evolution of the vertical emittance during the acceleration is shown in Fig. 7. In the Z mode, the final vertical beam emittance is much larger than the equilibrium vertical emittance at the extraction energy due to insufficient damping. In contrast, the final vertical beam emittance reaches the equilibrium vertical emittance in the W mode and H mode. The simulation agrees well with the

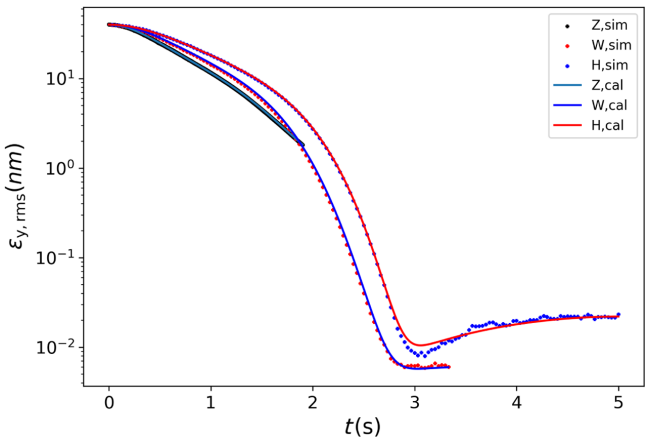

FIG. 7. The evolution of the simulated vertical rms emittance (in colored triangle symbols) and the calculated vertical rms emittance (in colored solid lines) using Eq. (40) during the acceleration for the three different operation modes. The error seed 001 in the collection is used, and the vertical equilibrium emittance is 21 pm at 120 GeV.

theoretical prediction of Eq. (40) for both the Z mode and W mode. There is some discrepancy at around $t = 3$ s between the simulation and the theory for the H mode, which can be attributed to the fact that the sawtooth effect is not included in Eq. (40). The above observation also holds for most other error seeds. In the estimation of depolarization effects described later in this paper, we used Eq. (40) to obtain the evolution of vertical rms emittance, as a reasonably good approximation.

IV. STRUCTURE OF SPIN RESONANCES FOR THE CEPC BOOSTER LATTICE

The general lattice structure and the setup of error seeds have already been introduced in Sec. III. Table IV lists lattice parameters relevant for analyzing the structure of spin resonances for the CEPC booster lattice.

The locations of superstrong spin resonances can be identified by using the analysis for the simple model ring in Sec. II C. Superstrong intrinsic resonances are located at $K = 8n \pm 353.28$, $n \in \mathbb{Z}$ near $K = 1136m \pm 284$, $m \in \mathbb{Z}$. As these two conditions cannot be met simultaneously, and the enhancement function $\zeta_M(\frac{K\eta_{\rm arc} \mp \nu_B}{PM})$ varies slowly with K near the peak, the first superstrong intrinsic resonance is located at $K = 281.28 = -9P + \nu_y$, corresponding to a beam energy of 123.9 GeV, where the enhancement amplitude $|E_P^- E_M^-|$ is 924. On the other hand, superstrong imperfection resonances are generally those where both conditions $K = 8n \pm 353$, $n \in \mathbb{Z}$ and $K = 1136m \pm 284$, $m \in \mathbb{Z}$ are nearly satisfied. The first superstrong imperfection resonance is located at $K = 281 = -9P + [\nu_y]$. Both the first superstrong imperfection and intrinsic resonances are located beyond the working beam energy range of the CEPC booster. Nevertheless, the resonances just below 120 GeV are still near the superstrong resonances and are enhanced. For example, the enhancement amplitude $|E_P^- E_M^-|$ is 127 at the intrinsic resonance $K = 265.28 = -11P + \nu_y$, corresponding to a beam energy of 116.9 GeV. In addition, the strength of intrinsic and imperfection resonances generally increases with the beam energy in the range of 10 to 120 GeV.

To verify the above analysis, we calculated the strengths of the intrinsic and imperfection resonances numerically and now discuss their features. We then analytically estimated the depolarization due to the crossings of these resonances.

TABLE IV. Key lattice parameters relevant to the structure of spin resonances.

Vertical tune ν_y	353.28
Superperiod P	8
Number of FODO cells in each arc section M	140
Proportion of total arc bending angle $\eta_{\rm arc}$	140/142
Contribution to ν_y from all arc sections ν_B	280
Number of FODO cells in each straight section M'	24
Contribution to ν_y from all straight sections $\nu_{y,\rm str}$	48
Number of FODO cells in each DOM section M''	6

A. Intrinsic resonances

To calculate the strength of intrinsic resonances, we used the DEPOL code [24] for the bare lattice and the sawtooth effect was not taken into account. As the strength of an intrinsic resonance depends on a particle's vertical betatron action I_y, we calculated using a normalized vertical amplitude $\epsilon_{y,\rm norm} = 2\gamma I_y$ of 10πmm mrad. The resulting intrinsic-resonance spectrum is shown in Fig. 8. In Fig. 8(a), where a large energy range is covered, the locations of superstrong intrinsic resonance are labeled by the positions of their peaks. These agree well with our analysis. Figure 8(b) shows the intrinsic-resonance spectrum in the working beam energy range. It is clear that the first

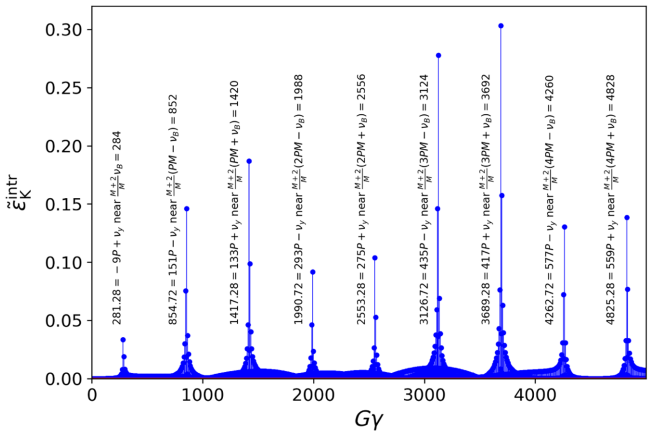

(a) In a large energy range

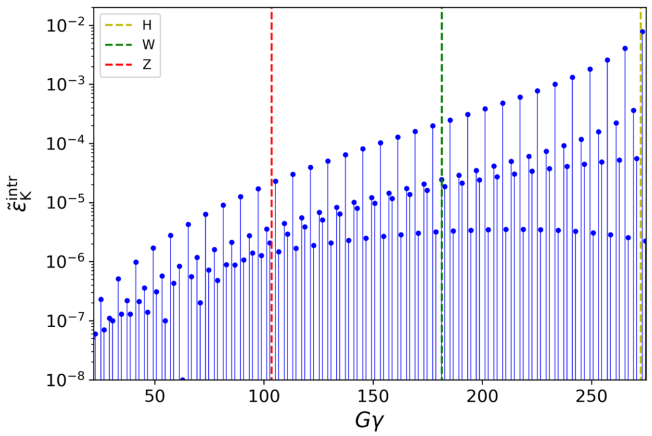

(b) In the working beam energy range

FIG. 8. Intrinsic-resonance spectrum of the bare lattice for a vertical normalized amplitude of 10π mm mrad. (a) A larger energy range with the locations of superstrong intrinsic resonances labeled. (b) The working energy range with the three extraction energies marked by dashed lines.

superstrong intrinsic resonance is above 120 GeV, below which the resonance strength generally increases with energy. Note that the minor differences in the DOM sections effectively reduce the periodicity from 8 to 4, resulting in the adjacent intrinsic resonances spaced by 4 units of $G\gamma$.

As the strength of an intrinsic resonance varies among particles with different vertical betatron amplitudes in a beam, different particles suffer from different levels of depolarization after crossing an intrinsic resonance at the same resonance crossing rate. So, to evaluate the beam depolarization, Eq. (4) must be extended with an ensemble average over particles with different vertical betatron amplitudes for a fixed α. For a Gaussian beam with an rms vertical emittance of $\epsilon_{y,\mathrm{rms}}$, the depolarization when crossing a single intrinsic resonance at $\nu_0 = K$ is [51]

$$\frac{P_f}{P_i}(K, \epsilon_{y,\mathrm{rms}}, \alpha) = \frac{1 - \frac{\pi|\tilde{\epsilon}_K^{\mathrm{intr},\pm}(\epsilon_{y,\mathrm{rms}})|^2}{\alpha}}{1 + \frac{\pi|\tilde{\epsilon}_K^{\mathrm{intr},\pm}(\epsilon_{y,\mathrm{rms}})|^2}{\alpha}} \tag{41}$$

Many intrinsic resonances would be crossed in the acceleration process. For an initial 100% vertically polarized beam, the vertical beam polarization at a certain time t during the acceleration $P_{\mathrm{trans}}^{\mathrm{intr}}(t)$ can be approximated by multiplying together the surviving polarization due to each intrinsic resonance the beam encounters before the time t,

$$P_{\mathrm{trans}}^{\mathrm{intr}}(t) \approx \prod_{K \le G\gamma(t)} \frac{P_f}{P_i}(K, \epsilon_{y,\mathrm{rms}}, \alpha) \tag{42}$$

Then, the final polarization after the acceleration is $P_{\mathrm{trans},f}^{\mathrm{intr}} = P_{\mathrm{trans}}^{\mathrm{intr}}(t_{\mathrm{ramp}})$.

As shown in Fig. 5, the vertical equilibrium emittance at a beam energy of 120 GeV $\epsilon_{y,\mathrm{eq},0}$ varies among different error seeds, in the range of 6 pm to about 500 pm. The vertical rms emittance also varies during the acceleration process as shown in Fig. 7. So we chose a vertical equilibrium emittance of 100 pm at 120 GeV and evaluated the evolution of the vertical rms emittance during the acceleration process according to Eq. (40). For each intrinsic resonance in the working beam energy range, we scaled its strength according to the vertical rms emittance at the time of crossing, as shown in Fig. 9(a). Using Eq. (4) and the spin-resonance crossing rate according to Eq. (38), we obtained the upper strength limit for each intrinsic resonance needed to ensure the depolarization due to its crossing of less than 1%. This is represented as the orange curve in Fig. 9(a). When compared with the spectrum of scaled intrinsic resonances, it is clear that only three intrinsic resonances near 120 GeV can cause severe depolarization.

Next, we scanned a range of vertical equilibrium emittance $\epsilon_{y,\mathrm{eq},0}$ at a beam energy of 120 GeV. For each case, we used Eq. (40) to evaluate the vertical rms emittance evolution during the acceleration. Then we used

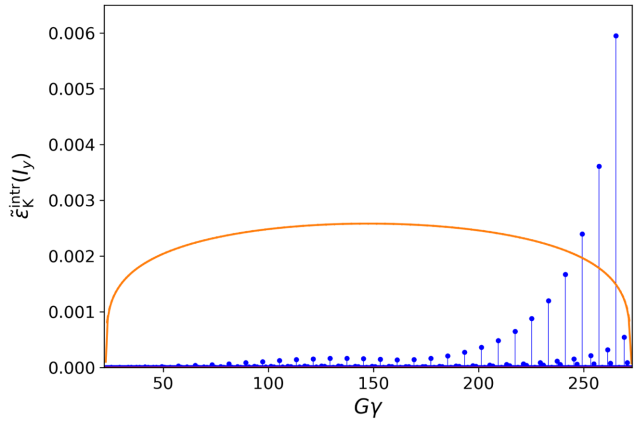

(a) Spectrum of scaled intrinsic resonances

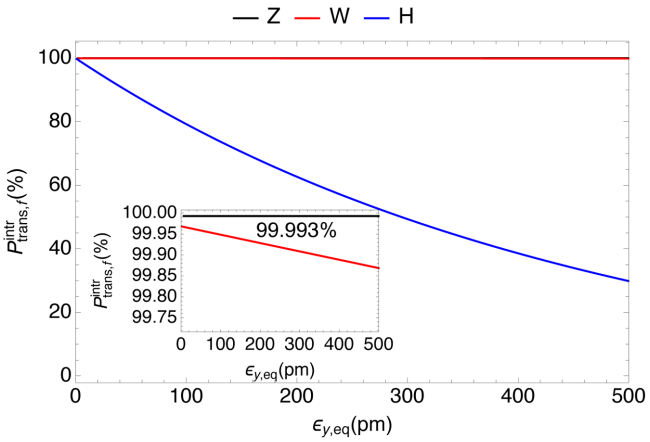

(b) Depolarization due to intrinsic resonances

FIG. 9. (a) Intrinsic-resonance spectrum in the working beam energy range, scaled using the vertical rms emittance at the time of resonance crossing, assuming a vertical equilibrium emittance of 100 pm at 120 GeV. The orange line depicts the estimated upper strength limit for each intrinsic resonance needed to ensure the depolarization due to its crossing of less than 1%. (b) Estimated final vertical polarization after crossing all the intrinsic resonances during the acceleration process, for different vertical equilibrium emittances $\epsilon_{y,\mathrm{eq}}$ at 120 GeV, and for the three operation modes. The inset plot shows an enlarged view of the results of the Z mode and the W mode, with tiny depolarization. In contrast, the H mode suffers from more severe depolarization, in particular, for a larger $\epsilon_{y,\mathrm{eq}}$.

Eq. (42) to estimate the polarization loss after crossing all intrinsic resonances in the acceleration process. The spin-resonance crossing rate was computed with Eq. (38). The results for the three operation modes are shown in Fig. 9(b). In the Z mode, the vertical rms emittance remains far from reaching the vertical equilibrium emittance during the short ramping time, and the change in the evolution of the beam vertical rms emittance is small for the range of $\epsilon_{y,\mathrm{eq}}$ we considered. In addition, the strengths of intrinsic resonances are generally small, resulting in a polarization loss of less than 0.01% and a slow variation as a function of $\epsilon_{y,\mathrm{eq}}$. However, in the W mode and H mode, the vertical rms

emittance reaches $\epsilon_{y,\mathrm{eq}}$ during acceleration and the polarization loss increases with $\epsilon_{y,\mathrm{eq}}$. The polarization loss in the W mode is still less than 0.15%, while the polarization loss in the H mode depends strongly on $\epsilon_{y,\mathrm{eq}}$, and exceeds 20% for $\epsilon_{y,\mathrm{eq}}$ larger than 100 pm, mainly due to the crossings of several strong intrinsic resonances before 120 GeV. This highlights the importance of reducing $\epsilon_{y,\mathrm{eq}}$ to small values through optics correction to minimize the depolarization caused by intrinsic resonance crossings.

B. Imperfection resonances

To calculate the strengths of imperfection resonances for different error seeds, we implemented the algorithm of the DEPOL code [24] in a *Mathematica* script [63] using the closed orbit and optics functions calculated by Bmad, where the sawtooth effect was not taken into account. The calculation took into account the major contributions due to quadrupoles, bends, and sextupoles, as well as corrector fields inside the quadrupoles, but did not consider the magnet roll errors nor the dipole relative field errors.

Figure 10(a) shows the imperfection-resonance spectrum in a large energy range for error seed 001 with a vertical rms COD of 97 μm. The locations of the superstrong imperfection resonances mostly agree with our previous analysis, apart from a few peaks corresponding to $|k| \neq [\nu_y]$. Since the strength of an imperfection resonance is a superposition of various Fourier terms of the vertical COD, there is, in addition, a broad "background" near each of these superstrong resonances. Figure 10(b) illustrates the imperfection-resonance spectra for three error seeds with different vertical rms CODs in the working energy range. The strength of imperfection resonances generally increases with energy, with 120 GeV just below the first strong imperfection resonance. Besides, it is clear there is an increase in the strength of the strongest imperfection resonance just below 120 GeV for error seed 060 with the largest vertical rms COD.

Unlike intrinsic resonances, the strength of an imperfection resonance is the same for all the particles in a beam so that the polarization loss due to crossing an isolated imperfection resonance can be estimated directly using Eq. (4). For each imperfection resonance, we calculated the upper strength limit for which the depolarization due to its crossing is less than 1%, considering the resonance crossing rate as shown in Fig. 6. We then obtained three curves of the upper strength limit for each imperfection resonance, colored in green, magenta, and brown for the Z mode, W mode, and H mode in Fig. 10, respectively. These curves can be compared with the strengths of imperfection resonances to identify the most dangerous resonances whose strengths lie above these curves. Clearly, the imperfection resonances near the extraction energies have larger strengths but are crossed at a lower speed, potentially causing more severe depolarization. For the Z mode, all

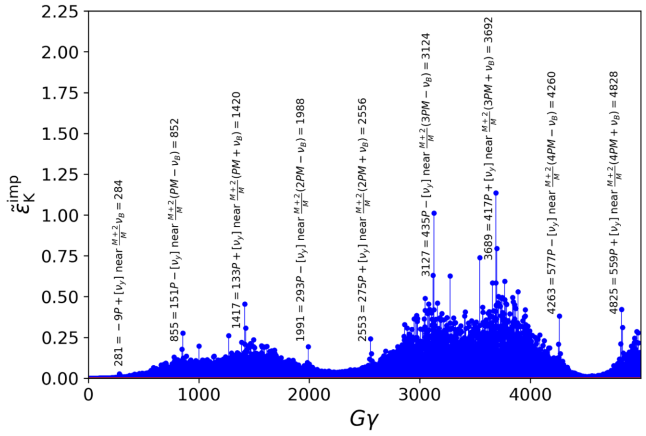

(a) In a large energy range

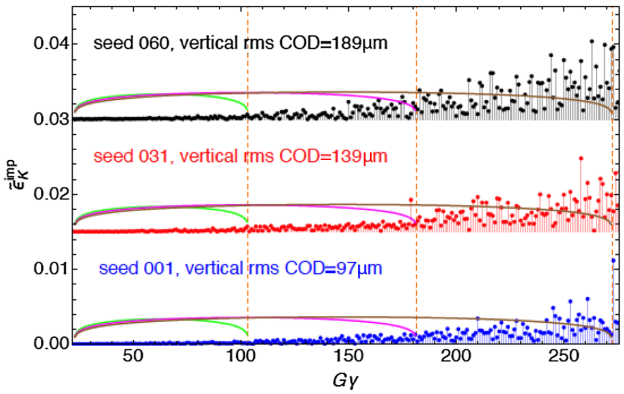

(b) In the working beam energy range

FIG. 10. Imperfection-resonance spectra of several error seeds of the CEPC booster lattice. (a) Imperfection-resonance spectrum of error seed 001 in a large energy range, highlighting the locations of superstrong imperfection resonances. (b) Imperfection-resonance spectra of error seed 001, 031, and 060 with increasing vertical rms CODs in the working energy range, an offset of 0.015 is appended to the latter two cases for comparison. The three dashed vertical lines denote the three extraction energies. The green, magenta, and brown curves depict the upper strength limit for each imperfection resonance needed to ensure the depolarization due to its crossing of less than 1%, for the Z mode, and W mode, H mode, respectively.

imperfection resonances in the three error seeds are below the green curve. For the W mode, the strengths of only a few imperfection resonances in error seeds 031 and 060 lie above the magenta curve, while the strengths of all imperfection resonances in error seed 001 are below the magenta curve. In contrast, for the H mode, the strengths of a significant number of imperfection resonances lie above the brown curve for the three error seeds, potentially causing substantial depolarization.

We quantify the depolarization due to the crossings of imperfection resonances, using a method similar to that for intrinsic resonances. For an initial 100% vertical polarization, we can estimate the vertical polarization at a specified

time t during acceleration, $P_{\mathrm{trans}}^{\mathrm{imp}}(t)$, by multiplying together the surviving polarization due to each imperfection resonance that the beam encounters before the time t,

$$P_{\mathrm{trans}}^{\mathrm{imp}}(t) \approx \prod_{K\le G\gamma(t)} \frac{P_f}{P_i}(K,\alpha) = \prod_{K\le G\gamma(t)} \left[2\exp\left(-\frac{\pi|\tilde{\epsilon}_K^{\mathrm{imp}}|^2}{2\alpha}\right)-1\right] \quad (43)$$

Then, the final vertical polarization after the acceleration for a time t_{ramp} is $P_{\mathrm{trans},f}^{\mathrm{imp}} = P_{\mathrm{trans}}^{\mathrm{imp}}(t_{\mathrm{ramp}})$. This implicitly assumes there is no correlation in the depolarization due to successive crossings of adjacent imperfection resonances.

We calculated the strengths of imperfection resonances for all 60 error seeds and estimated the depolarization due to the crossings of these imperfection resonances, for the three operation modes. The results, shown in Fig. 11, indicate that the polarization loss generally increases with the vertical rms COD. However, the polarization loss also varies among error seeds with similar vertical rms CODs, due to the difference in the spectra and maximum strengths of the imperfection resonances. For the Z mode and the W mode, the depolarization is less than 1% and 20%, respectively. In contrast, in the acceleration to 120 GeV, the depolarization is much more severe, ranging from about 50% to almost complete depolarization. This is due to the presence of many dangerous imperfection resonances near 120 GeV, as shown in Fig. 10.

In addition, the polarization loss due to these imperfection resonances is generally more severe than that caused by intrinsic resonances as estimated in the previous subsection. The next section will present an analysis of the combined effects of both imperfection and intrinsic resonances, as well as more realistic multiparticle simulation results of the beam depolarization in the acceleration process.

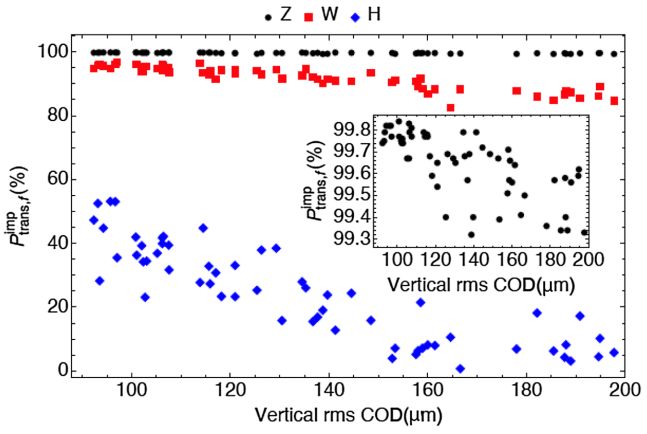

FIG. 11. Estimated final vertical beam polarization after crossing all the imperfection resonances during the acceleration process in the three operation modes, for the 60 error seeds with different vertical rms CODs. The inset plot shows an enlarged view of the result for the Z mode, with tiny depolarization. In contrast, the depolarization is more severe in the W mode and the H mode, especially for the error seeds with larger vertical rms CODs.

V. EVALUATION OF THE POLARIZATION TRANSMISSION

In this section, we present quantitative evaluations of the beam polarization transmission in the CEPC booster. Assuming the injected beam has a 100% vertical polarization, the evolution of the vertical beam polarization in the acceleration process, $P_{\mathrm{trans}}(t)$, and the final vertical beam polarization, $P_{\mathrm{trans},f}$, are evaluated using two different approaches.

In the previous section, we estimated the depolarization during acceleration in the CEPC booster, by separately considering the contributions of intrinsic resonances and imperfection resonances. By combining these two contributions, we can now estimate the overall depolarization effects due to both types of resonances,

$$P_{\mathrm{trans}}(t) \approx P_{\mathrm{trans}}^{\mathrm{intr}}(t) \times P_{\mathrm{trans}}^{\mathrm{imp}}(t) \quad (44)$$

and the final beam polarization after the acceleration is $P_{\mathrm{trans},f} = P_{\mathrm{trans}}(t_{\mathrm{ramp}})$. We applied such estimation for all the 60 error seeds and we used Eq. (38) to evaluate the evolution of beam energy and resonance crossing rate. For each error seed, we computed its vertical equilibrium emittance at a beam energy of 120 GeV $\epsilon_{y,\mathrm{eq},0}$, and then evaluated the evolution of the vertical rms emittance $\epsilon_{y,\mathrm{rms}}$ using Eq. (40). Note that the strengths of intrinsic resonances of these error seeds were approximated by those of the bare lattice as shown in Fig. 8. We scaled the strengths of intrinsic resonances during the acceleration process taking into account the evolution of $\epsilon_{y,\mathrm{rms}}$. In the following context, we refer to the $P_{\mathrm{trans},f}$ obtained using this method as the estimation results.

To verify our analysis, we utilized more realistic multiparticle tracking simulations of the acceleration process. For this, we used the "long_term_tracking" option of Bmad and we tracked a Gaussian beam of 1000 particles with an initial vertical polarization of 100%. We set the ramping curves of the beam energy and the rf parameters and turned on the radiation damping and quantum excitation effects in the element-by-element tracking with full six-dimensional orbit motion and three-dimensional spin motion. Hereafter, we refer to the $P_{\mathrm{trans},f}$ obtained using this method as the simulation results.

The estimates and simulation results of $P_{\mathrm{trans},f}$ for the 60 error seeds and the 3 operation modes are shown in Fig. 12. The simulation results for the Z mode and the W mode show maintenance of a high level of beam polarization,

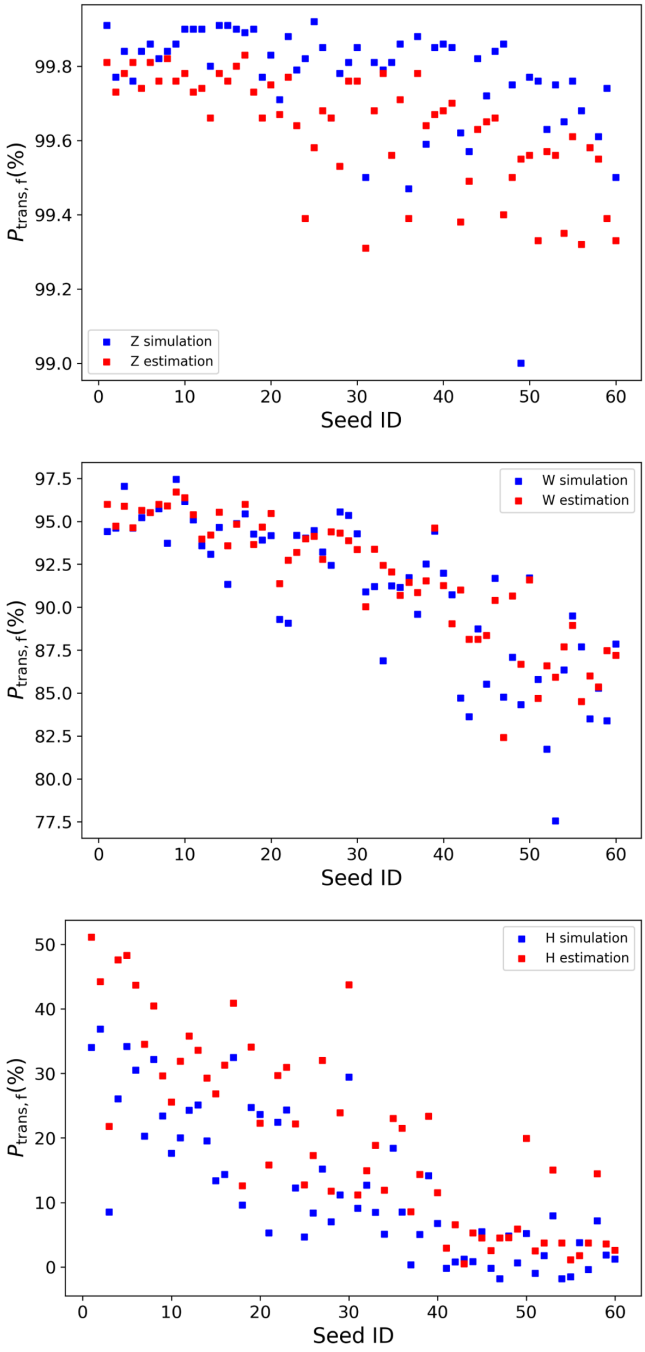

FIG. 12. The final beam polarization after the acceleration $P_{\mathrm{trans},f}$ for the 60 error seeds, assuming the injected beam is 100% vertically polarized. The top, middle, and bottom plots are for the Z mode, the W mode, and the H mode, respectively. The blue and red points represent the results of simulation and estimation, respectively.

with $P_{\mathrm{trans},f}$ mostly above 99% and 80%, respectively. In contrast, the simulation results for the H mode indicate substantial depolarization at higher beam energies, with $P_{\mathrm{trans},f}$ generally below 50%. The trend observed is that depolarization becomes more severe for larger seed IDs, whose vertical rms CODs are generally larger and imperfection resonances are generally stronger. The estimates of $P_{\mathrm{trans},f}$ are quite close to the simulation results, for the Z mode and the W mode, while the difference becomes more substantial for the H mode. It is worth noting that the estimation method used here, by simply multiplying together the surviving polarization due to each imperfection and intrinsic resonance, already provides a reasonably accurate order-of-magnitude estimate of $P_{\mathrm{trans},f}$. This suggests that single crossings of the imperfection and intrinsic resonances are the major factors of depolarization in CEPC booster.

To better appreciate the depolarization effects, the evolution of $P_{\mathrm{trans}}(t)$ in the acceleration process for a typical error seed 001 is illustrated in Fig. 13. Most polarization loss occurs near the end of the acceleration process when the ramping rate decreases while the resonance strengths become larger as the beam energy increases. Although the estimation results and simulation results of the $P_{\mathrm{trans},f}$ are generally similar, there are noticeable discrepancies in the evolution of $P_{\mathrm{trans}}(t)$. Next, we discuss several possible sources of the discrepancies.

First, the method of calculation we adopted for the strengths of spin resonances has limitations. For the calculation of the strength of imperfection resonances, the sawtooth orbit was not taken into account, nor were the magnet roll errors or the dipole relative field errors, which could lead to some discrepancies and affect the estimation of depolarization. Moreover, we used the strengths of intrinsic resonances for the bare lattice in the estimation of $P_{\mathrm{trans}}(t)$ for error seeds. The depolarization from intrinsic resonances is very weak for the Z mode and W mode, and the difference in the strength of intrinsic resonances does not affect the result much. However, the discrepancies between the bare lattice and the imperfect lattice could impact the results for the H mode. We are aware that the strengths of first-order spin resonances of error seeds can be more precisely calculated [35] within Bmad [57], this approach will be used in the future study of the depolarization effects in the H mode.

Second, the simulation results exhibit fluctuations in $P_{\mathrm{trans}}(t)$, most obvious in the Z mode, which are a signature of the interference-overlap effect [64] between the successive crossings of multiple adjacent imperfection resonances. This effect seems to be smeared out at higher beam energies due to the loss of coherence of the spin phase. One potential contributor is the stochastic change of particle energy due to synchrotron radiation, which was implemented on an element-by-element basis in the tracking with Bmad. In contrast, this effect was not taken into account in the estimates of depolarization, resulting in a monotonic decrease of $P_{\mathrm{trans}}(t)$ in the acceleration process.

Third, in our estimates, we only considered the depolarization due to single crossings of imperfection and intrinsic resonances. In contrast, the simulation results also take into account various more complicated depolarization effects, such as higher-order spin resonances, multiple

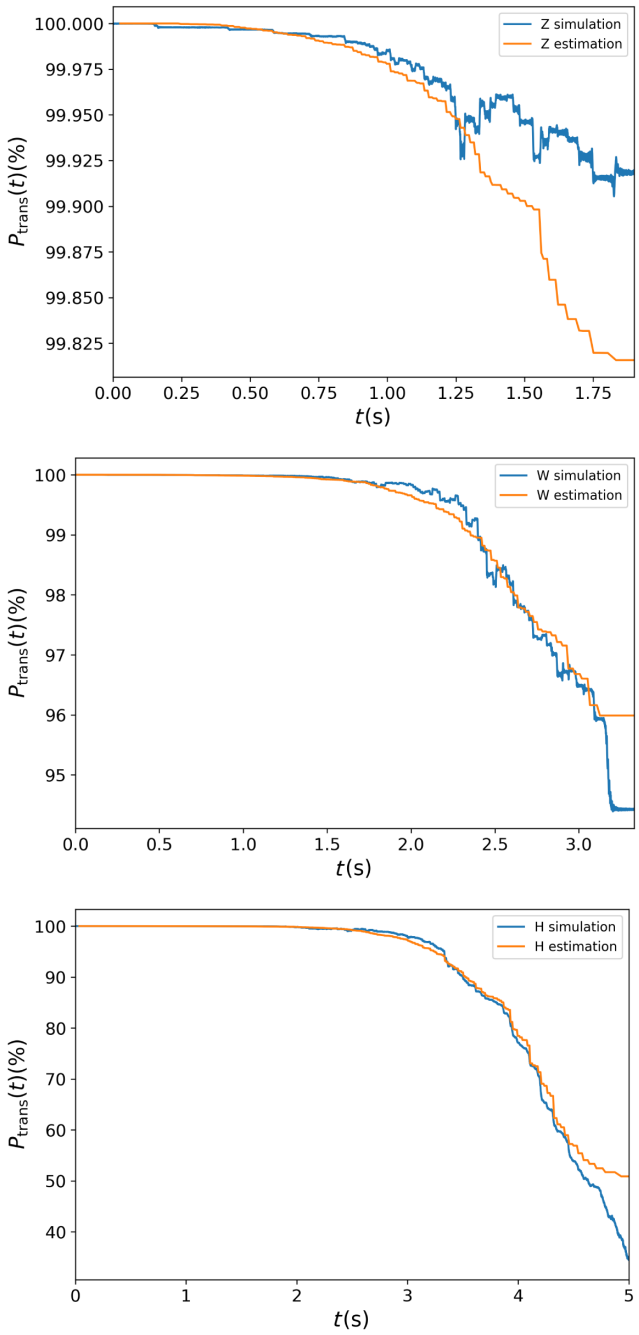

FIG. 13. Comparison between the simulated and estimated evolution of $P_{\mathrm{trans}}(t)$ for error seed 001 in the Z mode (top plot), the W mode (middle plot), and the H mode (bottom plot), respectively.

crossings of the same underlying spin resonances due to synchrotron oscillations [40,65], as well as radiative depolarization effects [40,54,66], etc. If we compare, for the Z mode and the W mode, the discrepancy between the estimates and simulation results, assuming they are mostly due to these alternative sources, then according to Figs. 12(a) and 12(b), we can estimate that their contribution to depolarization is no more than a few percent. However, it is more difficult to estimate their contribution to the H mode, as the discrepancy shown in Fig. 12(c) is much larger. A better understanding of these effects at higher energies near 120 GeV is needed and will be addressed elsewhere.

In addition, there is also a concern that the fluctuation of magnetic fields due to dynamic effects during the ramping process could cause additional depolarization. Dipole magnets, whose dynamic errors mostly affect the horizontal beam orbit, are typically powered in series, further reducing their influence. Dynamic errors of correctors and quadrupoles are more of concern. To this end, we added additional random field fluctuations to correctors and quadrupoles of up to 0.2%, to five error seeds from the collection with vertical rms CODs ranging from 100 to 180 μm and evaluated the influence to the polarization transmission for the Z mode and W mode. For each error seed and each amplitude of random field fluctuation, we generated 10 different random seeds of additional field errors. The variation in the polarization transmission is tiny for the Z mode and less than 3% for the W mode. Though random field fluctuations were implemented as fixed values rather than more realistic dynamic variations during the ramping process, these simulations show that polarization transmission is not sensitive to typical levels of additional field fluctuations, for the Z mode and W mode.

VI. CONCLUSION

This paper examines the depolarization effects during the acceleration process in the CEPC booster, from an injection energy of 10 GeV to the extraction energies of 45.6, 80, and 120 GeV, in the three operation modes, respectively. We used a simplified lattice for the CEPC booster, introduced machine imperfections, and launched closed-orbit correction and betatron-tune correction, generating 60 error seeds for evaluation of depolarization effects. We studied the structure of the imperfection and intrinsic spin resonances for a simplified lattice model analytically and then applied the analysis to the CEPC booster lattice. The locations of superstrong resonances and the general behavior of the resonance strengths in the working beam energy range were then verified with numerical calculations of the strengths of spin resonances for these 60 error seeds. The depolarization due to the crossings of these imperfection and intrinsic resonances were estimated using the Froissart-Stora formula and compared with the results of multiparticle tracking simulations of the acceleration process. These studies suggest that a high level of beam polarization can be maintained during the acceleration of 45.6 and 80 GeV, but severe depolarization could occur at higher beam energies in the acceleration of 120 GeV.

Our main finding is that the CEPC booster lattice has a high "effective" periodicity in terms of the lattice contributions to the strength of imperfection and intrinsic resonances, similar to that of the EIC booster [46]. Among imperfection and intrinsic resonances, superstrong

resonances, where the contributions of all arc FODO cells add up coherently, occur near $(mPM \pm \nu_B)/\eta_{\mathrm{arc}}, m \in \mathbb{Z}$. The spacings between adjacent superstrong resonances are very large, while the first superstrong resonances near $\nu_B/\eta_{\mathrm{arc}}$ also correspond to very high beam energies. Meanwhile, the contributions from a large number of FODO cells mostly cancel out for the resonances at much lower beam energies, away from the superstrong resonances. The key feature of the CEPC booster lattice is that all superstrong spin resonances are beyond the working beam energy range, though a few spin resonances near 120 GeV are still much enhanced. In fact, our test with several other candidate lattices of CEPC booster and collider rings confirmed that such a structure of spin resonances is a general feature of future 100-km-scale electron rings. This feature can be further exploited in the lattice design and optimization of these electron rings.

Apart from these underlying structure of spin resonances, the strengths of the imperfection resonances in the working beam energy range depend on the amplitude of radial magnetic fields around the ring, most importantly due to the vertical orbit offsets in quadrupoles. In this paper, we focus on the random misalignment errors of magnets and implemented closed-orbit correction to set a reasonable range of potential levels of COD, realized in past and existing machines, like the LEP [67]. Nevertheless, the systematic misalignment errors, due to variations in the vertical magnet positions after the smoothing procedure of alignment, or uneven settling of the accelerator floor over time, could also contribute to the radial magnetic fields and affect the strengths of imperfection resonances. This aspect requires a dedicated study and is beyond the scope of this paper. In addition, we are aware that dedicated orbit bumps can be set up to partially compensate certain strong imperfection resonances, namely, the harmonic closed-orbit spin matching [28,68,69], which shall also be pursued.

The sawtooth effect introduces nontrivial perturbations to the closed orbit and optics in the CEPC booster at higher beam energies. Its influence was taken into account in the simulation results of polarization transmission, but not in the calculation of strengths of imperfection and intrinsic resonances, and thus not in the estimation results. As the discrepancies between the simulation results and estimation results suggest, the influence of the sawtooth effect on depolarization is small for the Z mode and W mode, but can be more dramatic for the H mode. In practice, the perturbation to the closed orbit and optics as well as the spin resonance strengths due to the sawtooth effect during the acceleration process can be partly alleviated by "tapering" the magnetic field according to the local beam energy.

In contrast with the Z mode and W mode, it is more challenging to maintain the beam polarization in the acceleration to 120 GeV. For the booster lattice we studied in this paper, the polarization loss due to the intrinsic resonances could be reduced with a dedicated correction of the vertical equilibrium emittance while reducing the depolarization due to the imperfection resonances requires a better control of misalignment errors of quadrupoles, as well as improvements in the strategy of closed-orbit correction. Alternatively, the sensitivity of the lattice structure to misalignment errors in terms of the strengths of imperfection resonances should be studied, as an important ingredient in the lattice design and optimization. Nevertheless, even if the depolarization effects of the imperfection and intrinsic resonances can be well controlled, alternative depolarization sources, for example, the synchrotron oscillations and radiative depolarization effects could still cause depolarization near the extraction energy when the acceleration rate becomes lower. These effects as well as the optimization of the energy ramping curve require further investigations.

Maintaining beam polarization in the CEPC booster without the need for additional hardware, such as Siberian snakes, would immediately make injecting highly polarized beam(s) into the collider rings an attractive solution for RD measurements and longitudinally polarized colliding beam experiments. This approach has the potential of achieving a higher level of beam polarization, for both colliding and noncolliding pilot bunches, compared to using the Sokolov-Ternov effect in the collider rings. This work endorses a careful study of different aspects of this approach, specifically for Z and W energies.

ACKNOWLEDGMENTS

The authors are grateful to D. P. Barber for his helpful suggestions and careful reading of this manuscript, to S. Nikitin for discussions on experiments of polarized electron beam acceleration, to D. Sagan and E. Forest for their kind help with Bmad/PTC. This study was supported by National Key Program for S&T Research and Development (Grant No. 2018YFA0404300); National Natural Science Foundation of China (Grants No. 11975252 and No. 12275283); Youth Innovation Promotion Association CAS (No. 2021012).

[1] X. Lou, The Circular Electron Positron Collider, Nat. Rev. Phys. **1**, 232 (2019).
[2] The CEPC Study Group, CEPC Conceptual Design Report Volume I-Accelerator, arXiv:1890.00285.
[3] The CEPC Accelerator Study Group, Snowmass 2021 White Paper AF3-CEPC, arXiv:2203.09451.
[4] M. Benedikt and F. Zimmermann, The physics and technology of the Future Circular Collider, Nat. Rev. Phys. **1**, 238 (2019).
[5] S. Michizono, The International Linear Collider, Nat. Rev. Phys. **1**, 244 (2019).
[6] S. Stapnes, The Compact Linear Collider, Nat. Rev. Phys. **1**, 235 (2019).
[7] Y. S. Derbenev, A. M. Kondratenko, S. I. Serednyakov, A. N. Skrinsky, G. M. Tumaikin, and Y. M. Shatunov, Accurate calibration of the beam energy in a storage ring

based on measurement of spin precession frequency of polarized particles, Part. Accel. **10**, 177 (1980), https://inspirehep.net/literature/159462.

[8] R. W. Assmann *et al.*, Calibration of centre-of-mass energies at LEP1 for precise measurements of Z properties, Eur. Phys. J. C **6**, 187 (1999).

[9] Z. Duan, T. Chen, J. Gao, D. Ji, X. Li, D. Wang, J. Wang, J. Wang, Y. Wang, and W. Xia, Longitudinally polarized colliding beams at the CEPC, in *Proceedings of the 65th ICF Advanced Beam Dynamics Workshop on High Luminosity Circular e^+e^- Colliders, eeFACT 2022, Frascati, Italy* (JACoW, Geneva, Switzerland, 2022), pp. 97–102, https://doi.org/10.18429/JACoW-eeFACT2022-TUZAS0101.

[10] W. Xia, Z. Duan, J. Gao, and Y. Wang, Investigation of spin rotators in CEPC at the Z pole, Radiat. Detect. Technol. Methods **6**, 490 (2022).

[11] A. A. Sokolov and I. M. Ternov, On polarization and spin effects in the theory of synchrotron radiation, Sov. Phys. Dokl. **8**, 1203 (1964), https://inspirehep.net/literature/9147.

[12] A. Blondel, P. Janot, J. Wenninger *et al.*, Polarization and centre-of-mass energy calibration at FCC-ee, arXiv:1909.12245.

[13] A. Abada *et al.*, FCC-ee: The Lepton Collider, Eur. Phys. J. Spec. Top. **228**, 261 (2019).

[14] A. Brachmann, J. E. Clendenin, E. L. Garwin, K. Ioakeimidi, R. e. Kirby, T. Maruyama, C. Y. Prescott, J. Sheppard, J. Turner, and F. Zhou, The polarized electron source for the international collider (ILC) project, AIP Conf. Proc. **915**, 1091 (2007).

[15] E. Wang, O. Rahman, J. Skaritka, W. Liu, J. Biswas, C. Degen, P. Inacker, R. Lambiase, and M. Paniccia, High voltage dc gun for high intensity polarized electron source, Phys. Rev. Accel. Beams **25**, 033401 (2022).

[16] P. Musumeci, C. Boffo, S. S. Bulanov, I. Chaikovska, A. Faus Golfe, S. Gessner, J. Grames, R. Hessami, Y. Ivanyushenkov, A. Lankford, G. Loisch, G. Moortgat-Pick, S. Nagaitsev, S. Riemann, P. Sievers, C. Tenholt, and K. Yokoya, Positron sources for future high energy physics colliders, arXiv:2204.13245.

[17] M. Woods, The polarized electron beam for the SLAC Linear Collider, arXiv:hep-ex/9611006.

[18] G. Moortgat-Pick *et al.*, Polarized positrons and electrons at the linear collider, Phys. Rep. **460**, 131 (2008).

[19] L. H. Thomas, The kinematics of an electron with an axis, Philos. Mag. **3**, 13 (1927).

[20] V. Bargmann, L. Michel, and V. L. Telegdi, Precession of the Polarization of Particles Moving in a Homogeneous Electromagnetic Field, Phys. Rev. Lett. **2**, 435 (1959).

[21] D. P. Barber, J. Ellison, and K. Heinemann, Quasiperiodic spin-orbit motion and spin tunes in storage rings, Phys. Rev. ST Accel. Beams **7**, 124002 (2004).

[22] G. H. Hoffstaetter, H. S. Dumas, and J. A. Ellison, Adiabatic invariance of spin-orbit motion in accelerators, Phys. Rev. ST Accel. Beams **9**, 014001 (2006).

[23] A. W. Chao, Evaluation of beam distribution parameters in an electron storage ring, J. Appl. Phys. **50**, 595 (1979).

[24] E. D. Courant and R. D. Ruth, The acceleration of polarized protons in circular accelerators, BNL, Technical Report No. BNL 51270, 1980, https://doi.org/10.2172/7034691.

[25] Note that an integer spin resonance $\nu_0 = k$ can also be a "sideband" spin resonance of the "parent" first-order spin resonance $\nu_0 \pm \nu_z = k$ or of even higher-order "parent" spin resonances.

[26] M. Froissart and R. Stora, Depolarisation d'un faisceau de protons polarises dans un synchrotron, Nucl. Instrum. Methods **7**, 297 (1960).

[27] T. Khoe, R. L. Kustom, R. L. Martin, E. F. Parker, C. W. Potts, L. G. Ratner, R. E. Timm, A. D. Krisch, J. B. Roberts, and J. R. O'Fallon, Accelerator of polarized protons to 8.5 GeV/ct, Part. Accel. **6**, 213 (1975), http://cds.cern.ch/record/415893/files/p213.pdf.

[28] F. Z. Khiari *et al.*, Acceleration of polarized protons to 22 GeV/c and the measurement of spin-spin effects in $p\uparrow + p\uparrow \to p + p$, Phys. Rev. D **39**, 45 (1989).

[29] M. Bai *et al.*, Polarized Proton Collisions at 205 GeV at RHIC, Phys. Rev. Lett. **96**, 174801 (2006).

[30] M. Bai, Overcoming intrinsic spin resonances by using an RF dipole, PhD thesis, Indiana University, 1999.

[31] Y. S. Derbenev, A. M. Kondratenko, S. I. Serednyakov, A. N. Skrinsky, G. M. Tumaikin, and Y. M. Shatunov, Radiative polarization: Obtaining, control, using, Part. Accel. **8**, 115 (1978), https://s3.cern.ch/inspire-prod-files-3/3d1ba4e45a59386e2b20da3d307b636a.

[32] T. Roser, Properties of partially excited Siberian snakes, AIP Conf. Proc. **187**, 1442 (1989).

[33] H. Huang, L. A. Ahrens, M. Bai, K. Brown, E. D. Courant, C. Gardner, J. W. Glenn, F. Lin, A. U. Luccio, W. W. MacKay, M. Okamura, V. Ptitsyn, T. Roser, J. Takano, S. Tepikian, N. Tsoupas, A. Zelenski, and K. Zeno, Overcoming Depolarizing Resonances with Dual Helical Partial Siberian Snakes, Phys. Rev. Lett. **99**, 154801 (2007).

[34] V. Schoefer *et al.*, RHIC polarized proton operation in Run 12, in *Proceedings of the 3rd International Particle Accelerator Conference, New Orleans, LA, 2012* (IEEE, Piscataway, NJ, 2012).

[35] G. H. Hoffstaetter, *High-Energy Polarized Proton Beams*, edited by G. Höhler *et al.*, Springer Tracts in Modern Physics Vol. 218 (Springer, New York, 2006), https://doi.org/10.1007/978-0-387-34754-7.

[36] L. M. Barkov, I. B. Vasserman, P. V. Vorob'ev, P. M. Ivanov, G. Y. Kezerashvili, I. A. Koop, A. P. Lysenko, V. S. Okhapkin, A. A. Mikhaĭlichenko, E. A. Perevedentsev, A. A. Polunin, S. I. Redin, N. M. Ryskulov, A. N. Skrinskiĭ, V. P. Smakhtin, E. P. Solodov, B. I. Khazin, Y. M. Shatunov, and A. I. Shekhtman, Measurement of the properties of the ω meson with a cryogenic magnetic detector, JETP Lett. **46**, 164 (1987), https://inspirehep.net/literature/255953.

[37] S. Nakamura *et al.*, Acceleration of polarized electrons in ELSA, Nucl. Instrum. Methods Phys. Res., Sect. A **411**, 93 (1998).

[38] A. K. Barladyan, A. Y. Barnyakov, V. E. Blinov, S. A. Glukhov, S. E. Karnaev, E. B. Levichev, S. A. Nikitin, I. B. Nikolaev, I. N. Okunev, P. A. Piminov, A. G. Shamov, and A. N. Zhuravlev, Crossing integer spin resonance with conservation of beam polarization, Phys. Rev. Accel. Beams **22**, 112804 (2019).

[39] A. N. Zhuravlev, S. E. Karnaev, E. B. Levichev, O. I. Meshkov, S. A. Nikitin, I. B. Nikolaev, and P. A. Piminov, Current status of the VEPP-4 Accelerator Facility, Phys. Part. Nucl. Lett. **17**, 938 (2020).

[40] K. Yokoya, Effects of radiative diffusion on the spin-flip in electron storage rings, Part. Accel. **14**, 39 (1983), https://s3.cern.ch/inspire-prod-files-3/37d96b83535b80729c467570e22c91d9.

[41] I. Koop, A. Otboev, Y. Shatunov, and S. Mane, Acceleration of polarized electrons up to ultrahigh energies, Phys. Part. Nucl. Lett. **13**, 991 (2016).

[42] I. A. Koop, A. V. Otboev, and Y. M. Shatunov, Ideas for longitudinal polarization at the Z/W/H/top factory, in *Proceedings of the 62nd ICFA Advanced Beam Dynamics Workshop on High Luminosity, eeFACT 2018, Hong Kong, China* (JACoW, Geneva, Switzerland, 2018), WEXAA04, pp. 190–193, https://doi.org/10.18429/JACoW-eeFACT2018-WEXAA04.

[43] S. Nikitin, Opportunities to obtain polarization at CEPC, Int. J. Mod. Phys. A **34**, 1940004 (2019).

[44] S. Nikitin, Polarization issues in circular electron–positron super-colliders, Int. J. Mod. Phys. A **35**, 2041001 (2020).

[45] F. Willeke, Electron Ion Collider conceptual design report, Brookhaven National Laboratory (BNL), Upton, NY, Report No. BNL-221006-2021-FORE, 2021, https://doi.org/10.2172/1765663.

[46] V. H. Ranjbar, M. Blaskiewicz, F. Méot, C. Montag, S. Tepikian, S. Brooks, H. Witte, I. Marneris, V. Ptitsyn, and F. J. Willeke, Spin resonance free electron ring injector, Phys. Rev. Accel. Beams **21**, 111003 (2018).

[47] K. Yokoya, Beam polarization in high energy electron storage rings, KEK, KEK Report No. 85-7, 1986.

[48] Y. S. Derbenev and A. M. Kondratenko, Diffusion of particle spin in storage rings, Sov. Phys. JETP **35**, 230 (1972), https://inspirehep.net/literature/78600.

[49] G. H. Hoffstaetter and M. Vogt, Strength of higher-order spin-orbit resonances, Phys. Rev. E **70**, 056501 (2004).

[50] S. Y. Lee, Simple analytic formula for the strength of spin depolarizing resonances, AIP Conf. Proc. **145**, 189 (1986).

[51] S. Y. Lee, *Spin Dynamics and Snakes in Synchrotrons* (World Scientific, Singapore, 1997).

[52] S. R. Mane, Electron-spin polarization in high-energy storage rings. II. Evaluation of the equilibrium polarization, Phys. Rev. A **36**, 120 (1987).

[53] A physics picture that clarifies the integral of θ' from $-\infty$ is introduced in [54] using the concept of "anti-damping" [35].

[54] W. Xia, Z. Duan, Y. Wang, B. Wang, and J. Gao, Evaluation of radiative depolarization in the future circular electron-positron collider, arXiv:2204.12718.

[55] A. Terebilo, Accelerator toolbox for MATLAB, SLAC, Report No. SLAC-PUB-8732, 2001, https://doi.org/10.2172/784910.

[56] D. Sagan, Bmad: A relativistic charged particle simulation library, Nucl. Instrum. Methods Phys. Res., Sect. A **558**, 356 (2006).

[57] D. Sagan, The Bmad Reference Manual, https://www.classe.cornell.edu/bmad/manual.html (2023).

[58] K. Ohmi, K. Hirata, and K. Oide, From the beam-envelope matrix to synchrotron-radiation integrals, Phys. Rev. E **49**, 751 (1994).

[59] R. Assmann, P. Raimondi, G. Roy, and J. Wenninger, Emittance optimization with dispersion free steering at LEP, Phys. Rev. ST Accel. Beams **3**, 121001 (2000).

[60] A. Franchi, L. Farvacque, J. Chavanne, F. Ewald, B. Nash, K. Scheidt, and R. Tomás, Vertical emittance reduction and preservation in electron storage rings via resonance driving terms correction, Phys. Rev. ST Accel. Beams **14**, 034002 (2011).

[61] S. Y. Lee, *Accelerator Physics*, 2nd ed. (World Scientific, Hackensack, N.J, 2004), https://doi.org/10.1142/5761.

[62] D. Sagan, Long Term Tracking Program, https://www.classe.cornell.edu/bmad/manuals/long_term_tracking.pdf (2023).

[63] Wolfram Research, Inc., *Mathematica*, Version 12.0, Champaign, IL, 2020.

[64] A. W. Chao and E. D. Courant, Spin echo in synchrotrons, Phys. Rev. ST Accel. Beams **10**, 014001 (2007).

[65] T. Aniel, J. L. Laclare, G. Leleux, A. Nakach, and A. Ropert, Polarized particles at Saturne, J. Phys. (Paris), Colloq. **46**, 499 (1985).

[66] Y. Derbenev, A. M. Kondratenko, and A. N. Skrinsky, Radiative polarization at ultra-high energies, Part. Accel. **9**, 247 (1979), http://cds.cern.ch/record/1107967/files/p247.pdf.

[67] B. Dehning, J. Matheson, G. Mugnai, I. Reichel, R. Schmidt, F. Sonnemann, and F. Tecker, Beam based alignment at LEP, Nucl. Instrum. Methods Phys. Res., Sect. A **516**, 9 (2004).

[68] R. Rossmanith and R. Schmidt, Compensation of depolarizing effects in electron-positron storage rings, Nucl. Instrum. Methods Phys. Res., Sect. A **236**, 231 (1985).

[69] D. P. Barber *et al.*, High spin polarization at the HERA electron storage ring, Nucl. Instrum. Methods Phys. Res., Sect. A **338**, 166 (1994).